Atonal homolog 7 (ATOH7) loss-of-function mutations in predominant bilateral optic nerve hypoplasia

Atac, David ; Koller, Samuel ; Hanson, James V M ; Feil, Silke ; Tiwari, Amit ; Bahr, Angela ; Baehr, Luzy ; Magyar, István ; Kottke, Raimund ; Gerth-Kahlert, Christina ; Berger, Wolfgang

DOI: https://doi.org/10.1093/hmg/ddz268

Atonal homolog 7 *(ATOH7)* loss-of-function mutations in predominant bilateral optic nerve hypoplasia

David Grubich Atac[1], Samuel Koller[1], James V.M. Hanson[2], Silke Feil[1], Amit Tiwari[1], Angela Bahr[1], Luzy Baehr[1], István Magyar[1], Raimund Kottke[3], Christina Gerth-Kahlert[2], Wolfgang Berger[1,4,5,*]

[1]Institute of Medical Molecular Genetics, University of Zurich, 8952 Schlieren, Switzerland.

[2]Department of Ophthalmology, University Hospital Zurich and University of Zurich, 8091 Zurich, Switzerland.

[3]Department of Diagnostic Imaging, University Children's Hospital Zurich, 8032 Zurich, Switzerland.

[4]Zurich Center for Integrative Human Physiology, University of Zurich, 8057 Zurich, Switzerland.

[5]Neuroscience Center Zurich, University and ETH Zurich, 8057 Zurich, Switzerland.

**To whom correspondence should be addressed at:* Institute of Medical Molecular Genetics, University of Zurich, 8952 Schlieren, Switzerland. Tel: +41 44 556 33 50; Fax: + 41 44 556 33 51; Email: berger@medmolgen.uzh.ch

Abstract

Optic nerve hypoplasia (ONH) is a congenital optic nerve abnormality caused by underdevelopment of retinal ganglion cells (RGCs). Despite being a rare disease, ONH is the most common optic disc anomaly in ophthalmological practice. So far, mutations in several genes have been identified as causative, however many cases of ONH remain without a molecular explanation. The early transcription factor atonal basic-helix-loop-helix (bHLH) transcription factor 7 (*ATOH7*) is expressed in retinal progenitor cells and has a crucial role in RGC development. Previous studies have identified several mutations in the *ATOH7* locus in cases of eye developmental diseases such as nonsyndromic congenital retinal nonattachment and persistent hyperplasia of the primary vitreous.

Here we present two siblings with a phenotype predominated by bilateral ONH, with additional features of foveal hypoplasia and distinct vascular abnormalities, where whole-exome sequencing identified two compound heterozygous missense mutations affecting a conserved amino acid residue within the bHLH domain of *ATOH7* (NM_145178.3:c.175G>A; p.(Ala59Thr) and c.176C>T; p.(Ala59Val)). *ATOH7* expression constructs with patient single nucleotide variants were cloned for functional characterization. Protein analyses revealed decreased protein amounts and significantly enhanced degradation in the presence of E47, a putative bHLH dimerization partner. Protein interaction assays revealed decreased heterodimerization and DNA-binding of ATOH7 variants, resulting in total loss of transcriptional activation of luciferase reporter gene expression. These findings strongly support pathogenicity of the two *ATOH7* mutations, one of which is novel. Additionally, this report highlights the possible impact of altered ATOH7 dimerization on protein stability and function.

Introduction

Congenital visual impairment can be caused by optic nerve hypoplasia (ONH; OMIM #165550), which has been recognized as one of the most common causes of childhood blindness with a prevalence of 2.4-17.3 cases per 100 000 (1–3). ONH is the most common and severe type of congenital optic nerve anomaly, characterized by small, normal, grey or pale appearing optic nerves with a typical "double-ring sign" on funduscopy associated with abnormalities in size and distribution of the retinal vessels (4). It is estimated that approximately 80 % of patients suffering from bilateral ONH are legally blind, however the phenotype is highly variable and ranges from nearly normal vision to no perception of light (5). Although ONH does occur as an isolated trait, most cases are associated with developmental abnormalities such as anterior segmental defects of the eye, septo-optic dysplasia, hemispheric or pituitary abnormalities, developmental delay, and autism spectrum disorders (4,6–8).

ONH typically presents as sporadic cases, many of which remain without a clear molecular diagnosis. With advances in high-throughput sequencing technology over the past decade, several ONH-associated mutations have been reported, a majority of which occur in neural or retinal transcription factor genes (9). *HESX1* mutations have been identified as a rare cause of ONH with septo-optic dysplasia and hypopituitarism, but also documented in patients without ONH (10–13). *PAX6* mutations were described in patients with bilateral ONH as well as patients with unilateral or bilateral optic nerve aplasia (ONA) (6). *SOX2* mutations were found in several patients suffering from ONH and either brain malformations or microphthalmia/anophthalmia (8). Heterozygous *NR2F1* mutations have been detected in several patients suffering from Bosch-Boonstra-Schaaf Optic Atrophy Syndrome (BBSOAS), which includes ONH (14). Heterozygous mutations in *OTX2* are the second most common cause for microphthalmia/anophthalmia and approximately a third of these patients have ONH

(15,16). A homozygous missense variant in *VAX1* has also been reported in a patient with microphthalmia, ONH, and brain malformations (17).

Atonal basic helix-loop-helix (bHLH) transcription factor 7 (*ATOH7*) encodes a 152 amino acid protein, which forms a helix-loop-helix domain responsible for protein dimerization as well as a DNA-binding basic domain located within the first helix (18). The mouse ortholog *Math5* has been identified as a crucial factor in the development of the retina, specifying the differentiation of retinal ganglion cells (RGCs) from retinal progenitor cells (RPCs) (19). *Math5*$^{-/-}$ mice display normal sized eyes without optic nerves, chiasms, or RGCs but with an increased number of cone photoreceptors (20). Transgene expression of *ATOH7* in human induced pluripotent stem cells (hiPSCs) has been likewise demonstrated to drive differentiation of RGCs (21). Several SNPs in the 5'-UTR of *ATOH7* were found to be associated with optic disc size in a genome-wide association study (22).

ATOH7 is implicated in several developmental eye disorders. Mutations in a remote upstream transcription enhancer region of *ATOH7* were associated with nonsyndromic congenital retinal nonattachment (NCRNA; OMIM # 221900) (23,24). A missense point-mutation in the DNA-binding domain of *ATOH7* (p.(Asn46His)) was shown to lead to persistent hyperplasia of the primary vitreous (PHPV; OMIM #221900) (25). This replicates a previous finding in *Math5*$^{-/-}$ mice, in which lack of RGCs resulted in abnormal retinal vessel development and persistent hyaloid vasculature (20). A homozygous frameshift mutation in the *ATOH7* coding region has been identified in two Turkish siblings suffering from various developmental eye defects including, amongst others, microphthalmia, persistent fetal vasculature (PFV; OMIM #221900), ONH, and NCRNA (26). Khan et al. also described a severe phenotype in several affected members of a consanguineous family from Pakistan caused by a homozygous *ATOH7* missense mutation (p.(Glu49Val)). The phenotype involved microcornea,

microphthalmia, dense corneal opacities, retrolental mass, and severe retinal and vitreous dysplasia.

Although a potential link to ONH is implied by its occurrence as part of various global eye phenotypes caused by *ATOH7* mutations, the role of this transcription factor in ONH remains unclarified. In a study including 34 ONH patients with or without septo-optic dysplasia, six sequence variants were identified within the untranslated region of the *ATOH7* locus as well as one intronic variant (27), but no mutations in the coding region. In another study, Sanger sequencing of 12 patients suffering from ONH or ONA identified two heterozygous missense variants p.(Ala47Thr) and p.(Arg65Gly) in *ATOH7* (22). However, *in vitro* functional characterization could not confirm these variants as causative of the phenotype (25).

Here we present two compound heterozygous missense mutations in *ATOH7*, NM_145178.3:c.175G>A (p.(Ala59Thr)) and c.176C>T (p.(Ala59Val)), which segregate with an ocular phenotype dominated by bilateral ONH in a Swiss family with two affected siblings. Glial tissue was present in one of the patients. This may be interpreted as a variant of PFV. Findings of abnormal retinal vasculature, including tortuosity and incomplete peripheral vascularization (the far peripheral retina could only be examined in one patient), were present upon examination and may be an indirect result of the interruption of RGC development by the described *ATOH7* mutations. As Provis pointed out, the primary retinal vasculature develops at the RNFL/ RGC interface (28). Thus, a disturbance of this interface will interrupt retinal vessel development. This is evidenced clinically by the frequent association of optic disc anomalies with abnormal retinal vessel distribution.

Additionally, foveal hypoplasia (FVH) was present in the affected siblings as well as the father. A heterozygous missense single nucleotide variant (SNV) in *OPA3,* NM_001017989.2:c.43G>C (p.Gly15Arg), was found in all family members presenting with FVH and was proposed as an additional potential candidate for this finding. A detailed *in*

vitro functional assessment of the respective mutant ATOH7 proteins expressed in HEK293T cells was performed, addressing protein expression, stability, and function. As bHLH transcription factors primarily act as heterodimers with other bHLH proteins, the bHLH transcription factor E2-alpha isoform E47, encoded by the transcription factor 3 (*TCF3*) gene (29), was co-expressed as a putative binding partner in functional assays. Our findings indicate that the patient-derived *ATOH7* sequence variants ((p.(Ala59Thr) and p.(Ala59Val)), which affect a highly conserved amino acid residue within the helix-loop-helix (HLH) domain, have a significant impact on protein stability, heterodimerization, and DNA-binding, as well as a total loss of ATOH7-induced transcriptional activation. The presented ONH cases are the first report of compound heterozygous *ATOH7* missense mutations associated with a non-syndromic ocular phenotype dominated by ONH. Furthermore, this report highlights the impact of ATOH7 protein dimerization on protein stability and function. In the light of these observations, analysis of *ATOH7* in patients with isolated and sporadic ONH is highly recommended.

Results

Severe bilateral optic nerve hypoplasia and foveal hypoplasia in two siblings with poor vision

The index patient was referred to the Department of Ophthalmology at the University Hospital of Zurich at the age of seven years due to unexplained low vision despite corrective glasses and amblyopia treatment. The patient had a history of esotropia observed at the age of two-and-a-half years and myopic astigmatism observed at the age of four years. No extraocular manifestations were present. The index patient's younger sister was referred at the age of three due to reduced visual function. The patient had a history of esotropia at the age of two years. The two older siblings and the non-consanguineous parents of Caucasian ancestry had no history of visual disabilities. The affected children had no history of prematurity, were cognitively normal for their age, and had excellent grades at school during the observation period.

Initial examination of the index patient revealed best-corrected visual acuity at distance 20/100 (RE) and 20/200 (LE), and at near 20/80 (RE) and 20/100 (LE) at age seven years. Left microesotropia was present. Refraction showed myopic astigmatism. Examination of the younger affected sibling revealed that visual acuity at near was reduced to 20/200 (RE) and 20/100 (LE) at three years of age. Orthoptic assessment diagnosed a right microesotropia with eccentric fixation superior to the presumed foveola. Refraction showed hyperopic astigmatism. Neurological and endocrinological assessment was normal in both siblings. Visual acuity was stable during the observation period up to age 11 and six in the index patient and her sister, respectively. The remaining family members had a normal visual function and optic nerve development.

Dilated fundus examination of the index patient and her younger sister demonstrated bilateral severe ONH as well as signs of FVH and abnormal vessel distribution with tortuosity and drag of the retinal vessels towards the temporal side (Fig. 1A-B). Imaging of the peripheral retina revealed incomplete vascularization of the far peripheral retina, without visible signs of neovascularization, in the affected sibling (unfortunately the index patient was not available for further imaging) (Suppl. Fig. 1); for this reason, as well as the ages of the patients, no angiography was performed. There was no sign of microphthalmia or microcornea. Optical coherence tomography (OCT) revealed significantly reduced thickness of the retinal nerve fiber layer (RNFL) as well as the ganglion cell and inner plexiform layers (GCIPL) in the two affected siblings (Table 1). The index patient and her father showed also signs of grade one foveal hypoplasia with absent extrusion of plexiform layers and a shallow foveal pit (Fig. 1G and C, respectively), whereas the affected sibling showed grade two hypoplasia with absent extrusion of plexiform layers and absent foveal pit (Fig. 1H). Structural grading of foveal morphology was performed according to Thomas et al. (30). The other family members exhibited normal OCT findings of the optic nerve and macular region (Table 1; Fig. 1D-F).

Cerebral magnetic resonance imaging (MRI) of the index patient confirmed severely hypoplastic optic nerves within small optic nerve sheaths (Fig. 1I and J) in comparison to a control (Fig. 1K and L). No abnormalities of midline structures or other brain areas were observed. No MRI was performed on the affected younger sibling because of the similarity between her fundus changes and those of her sister, her normal developmental state, and because successful MRI scan acquisition would have required sedation due to her age.

Compound heterozygous *ATOH7* missense variants segregate with optic nerve hypoplasia

Whole exome sequencing (WES) of the index patient and the affected sister revealed two biallelic missense variants in the bHLH domain of *ATOH7*: NM_145178.3:c.175G>A;

p.(Ala59Thr) and c.176C>T; p.(Ala59Val), of which p.(Ala59Thr) is not present in genome databases and p.(Ala59Val) is a rare variant with a minor allele frequency (MAF) of one in 25 000 in non-Finnish European population (NFE). No other rare variants were detected in a gene panel consisting of a total of 29 genes (Suppl. Table 1) previously associated with ONH (8,10,14,16,17,26,31–46) and/or FVH (40,47–51).

The discovered *ATOH7* variants segregated with optic nerve hypoplasia within the family (Fig. 2A). Sanger sequencing confirmed compound heterozygosity in the affected siblings and presence of heterozygous variants in the unaffected family members (Fig. 2B). The unaffected parents as well as the two unaffected siblings were all carriers of either of the two variants. Both variants were predicted likely to be disease causing by three different algorithms (Table 2), affecting a highly conserved amino acid residue within the first helix of the bHLH domain of *ATOH7* (Suppl. Fig. 2). High-throughput sequencing of a 9.3 kb long-range PCR product spanning the entire *ATOH7* locus was performed on all family members and excluded additional rare sequence variants, in introns as well as in flanking regions.

Genetic testing for foveal hypoplasia in the father

The father of the two affected siblings revealed FVH upon OCT examination. This was also seen in the two affected siblings. In order to investigate whether there was an independent genetic reason for this finding in the father, we performed WES. As no additional rare variants were found in candidate genes associated with ONH and/or FVH (Suppl. Table 1), the gene list was extended to include our institute's gene panel for eye diseases (https://www.medmolgen.uzh.ch/de/services/Hauptgene.html; accessed 01.07.2019). The extended filtering revealed a rare heterozygous *OPA3* exon one sequence variation, with a MAF of one in 100 000 in the NFE population, which was discovered in the father (NM_001017989.2: c.43G>C; p.(Gly15Arg)) and was also present in the affected siblings. Sanger sequencing of this *OPA3* variant revealed that the unaffected older sister was also a

carrier (Suppl. Fig. 3). The *OPA3* variant was predicted likely to be disease causing by three different algorithms (Table 2). However, since it is also present in the unaffected sister, it may not be the causative sequence variant for the clinical feature of foveal hypoplasia in this family. Alternatively, incomplete penetrance may explain the unaffected mutation carrier.

Reduced protein amounts of ATOH7 variants in the presence of a dimerization partner

Protein amounts of transgenic V5-tagged ATOH7 in HEK293T cells were measured by semi-quantitative western blot (Fig. 3 and Suppl. Fig. 4). To simulate heterozygosity, both patient-derived variants were co-expressed with wildtype ATOH7. The previously characterized *ATOH7* mutation p.(Asn46His) was included in the experiments as a loss-of-function control (25). As an additional control, an artificial missense variant (NM_145178.3:c.176C>G; p.(Ala59Gly)) was constructed, with high biochemical similarity of the substituted amino acid residue to its wildtype counterpart.

No statistically significant difference in variant protein amount was detected in comparison to wildtype ATOH7 (Fig. 3A). The bHLH transcription factor E2-alpha isoform E47, encoded by *TCF3*, represents a putative dimerization partner of ATOH7 (25). In the presence of co-expressed E47, a significant decrease in protein amounts of patient variants was observed relative to wildtype ATOH7, suggesting reduced protein stability of ATOH7 when forming heterodimers with E47 (Fig. 3B). Reduced amounts were observed to a lesser degree for the artificial variant, the loss-of-function control p.(Asn46His), as well as for the patient variants co-expressed with wildtype ATOH7. Treatment with proteasome inhibitor MG-132 completely restored the relative ATOH7 variant protein amounts (except for p.(Ala59Val)) when co-expressed with E47 (Fig. 3D), suggesting proteasome-dependent degradation.

Co-expression of E47 increases proteasome-mediated degradation of variant ATOH7 protein

Cycloheximide (CHX) time course assays were performed in order to verify the suggested increased protein turnover of ATOH7 variants (Fig. 4 and Suppl. Fig. 5). HEK293T expressing V5-tagged ATOH7 were pretreated with CHX to block protein synthesis, and protein amounts were quantified by western blot at time points zero to four hours post CHX addition. No significant difference in protein stability was observed for any of the ATOH7 variants in the absence of the putative dimerization partner E47 (Fig. 4A), while co-expression of E47 significantly increased the turnover rate of the ATOH7 patient variants. The loss-of-function variant p.(Asn46His) and the synthetic variant p.(Ala59Gly) demonstrated similar turnover rates, which were significantly increased compared to wildtype ATOH7 but significantly slower compared to ATOH7 patient variants (Fig. 4B). Treatment with MG-132, an inhibitor of proteasomal degradation, resulted in normalization of all protein variant turnover rates relative to wildtype ATOH7. This confirmed proteasome-mediated degradation as the main mechanism for reduced protein amount of ATOH7 variants in presence of a putative dimerization partner (Fig. 4D).

Reduced heterodimerization of patient-derived ATOH7 with E47

Protein-protein interaction ELISA was performed in order to investigate the potential impact of ATOH7 patient variants on bHLH protein dimerization. No significant enrichment of either V5-tagged wildtype or variant ATOH7 could be detected when exposed to antibody immobilized c-Myc-tagged ATOH7 protein (Fig. 5A-B). A significant enrichment of V5-tagged wildtype ATOH7 was detected in the presence of antibody immobilized c-Myc-tagged E47 (Fig. 5C), representing ATOH7-E47 heterodimer formation *in vitro*. The loss-of-function variant p.(Asn46His) as well as the combination of the p.(Ala59) patient variants did not show

significant heterodimerization compared to background control. All ATOH7 variants exhibited significantly reduced heterodimerization compared to wildtype ATOH7.

Patient-derived ATOH7 variants show reduced DNA-binding

To address the impact on DNA-binding ability of the ATOH7 variants, a DNA-protein interaction enzyme-linked immunosorbent assay (ELISA) was established. Double-stranded DNA containing seven consecutive canonical E-box sequences (CAGGTG) was immobilized to immunoassay plates by biotin-streptavidin interaction. HEK293T lysate containing transgenic V5-tagged ATOH7 was incubated with or without lysate containing E47. In concordance with dimerization assays, no DNA-binding of V5-tagged wildtype or variant ATOH7 protein could be detected in the presence of immobilized E-box (Fig. 6A). A significant E-box dependent DNA-binding was observed with wildtype ATOH7 in the presence of E47, suggesting DNA-binding of ATOH7-E47 heterodimers (Fig. 6B). Except for the synthetic variant p.(ala59Gly), all ATOH7 protein variants exhibited significantly reduced DNA-binding compared to wildtype ATOH7. DNA-binding of the combination of p.(Ala59) variants, as well as the previously published p.(Asn46His), did not show significant enrichment compared to negative control (scrambled E-box), suggesting potential loss of DNA-binding ability. Additionally, the p.(Asn46His) showed significantly lower enrichment compared to all other tested variants.

***ATOH7* patient-derived protein variants represent loss-of-function mutations**

Since the biological function of ATOH7 is transcriptional activation or regulation of target genes, we performed reporter gene assays. Dual luciferase assays were carried out in HEK293T in order to investigate whether or not the ATOH7 patient-derived variants are capable of transcriptional activation. HEK293T were transfected with plasmid constructs carrying the firefly luciferase reporter gene regulated by a minimal promoter containing seven canonical E-box sequences.

Assessment of cells co-expressing wildtype ATOH7 displayed a significant increase of luciferase expression over background, which was further enhanced by co-expressing E47 (Fig. 7A), indicating functional ATOH7-E47 dimers. In contrast, patient-derived ATOH7 protein variants did not show a statistically significant transcriptional activation of reporter gene expression, regardless of co-expression with E47. Similarly, the loss-of-function variant p.(Asn46His) did not show any transcriptional activation, which is consistent with previously published data (25). Interestingly, a significant decrease of base level luciferase activity could be seen when expressing p.(Asn46His) in presence of E47.
The artificial variant p.(Ala59Gly) displayed statistically significant transcriptional activation, however this was reduced in magnitude relative to wildtype ATOH7 (Fig. 7B). Co-expression of wildtype ATOH7 and patient variants, mimicking the carrier status of the parents, displayed a minor reduction in luciferase reporter expression compared to wildtype ATOH7. In order to account for potentially reduced ATOH7 variant protein expression when co-expressing E47, luciferase assays were also carried out on MG-132 treated samples (Suppl. Fig. 6). The loss of transcriptional activation of the ATOH7 patient variants remained. Confocal microscopy of fluorescently stained V5-tagged ATOH7 was additionally performed in order to verify that the measured loss of transcriptional activation is not due to protein mislocalization. The patient ATOH7 variants retained their nuclear localization (Suppl. Fig. 7).

Discussion

Patient-derived ATOH7 variants affect protein heterodimerization

ATOH7 is a class II bHLH transcription factor, characterized by tissue specific expression, low capability of homodimerization, and favored heterodimerization with class I bHLH transcription factors, also known as E proteins (52). The latter characteristics support our observation that wildtype ATOH7 protein could not be enriched in ELISA assays through protein homodimerization (Fig. 5) nor through E-box DNA-binding (Fig. 6) in the absence of the putative heterodimerization partner E47. This finding is supported by the results of previous work by Prasov et al., who observed ATOH7-E47 protein heterodimers but not ATOH7 homodimers by means of electrophoretic mobility shift assay (EMSA) (25). Interestingly, we were able to measure E-box mediated transcriptional activation induced by wildtype ATOH7 in the absence of E47 co-expression (Fig. 7). It is likely that endogenously expressed E47 and/or other class I bHLH binding partners may have contributed to transcriptional activation through heterodimerization with transgenic ATOH7. It is also possible that short-lived functional homodimers are stable inside the nucleus of a living cell but not in cell-free conditions.

Our findings suggest that the two characterized *ATOH7* missense variants at protein position 59 lead to significantly reduced heterodimerization. The 59th amino acid position of ATOH7 is a highly conserved residue within the HLH domain, important for bHLH transcription factor dimerization. A closely related homolog of *ATOH7* is the class II bHLH transcription factor *NEUROD1*. The crystal structure of the E47-NEUROD1 heterodimer has been previously identified through x-ray crystallography (53). The alanine at the 59th position of ATOH7 coincides with alanine at position six of the first helix in the NEUROD1 amino acid sequence (Suppl. Fig. 8), which has been identified to be part of the E47-NEUROD1 dimer

interface and thus supports our finding that mutations in this position have a deleterious impact on heterodimerization.

Interestingly, the previously described loss-of-function variant p.(Asn46His) did not show significant heterodimerization, despite being located within the DNA-binding basic domain of ATOH7 and thus outside of the HLH domain. It is possible that the substitution of asparagine for histidine, which introduces an imidazole ring and thus a net positive charge of the amino acid residue, may influence the secondary protein structure and thus the overall ability of the variant ATOH7 monomer to form dimers with E47.

ATOH7 heterodimerization affects DNA-binding and transcriptional activation

Interestingly, both of the patient-derived *ATOH7* variants also resulted in decreased/lost ability of the ATOH7 protein to bind E-box DNA (Fig. 6), despite the fact that these amino acid substitutions are located outside the DNA-binding basic domain. This may be explained as a direct consequence of impaired and decreased heterodimerization, which disrupts DNA-binding of bHLH proteins (54). These functional aberrations ultimately lead to loss of transcriptional activation of the two ATOH7 patient-derived variant proteins, as observed in luciferase reporter assays (Fig. 7).

The artificial ATOH7 p.(Ala59Gly) variant was used as a control throughout the functional characterization. Due to the similar properties of alanine and glycine, we expected little or no impact on protein function. The variant displayed reduced dimerization and DNA-binding, however transcriptional function/activation was retained and this variant may therefore be considered a hypomorphic allele.

In contrast, the published p.(Asn46His) variant, located in the DNA-binding basic domain, failed to bind DNA and activate transcription. This is in concordance with previously reported functional characterization (25) as well as the crystal structure of E47-NEUROD1 identifying

the amino acid position to be an important residue contributing to DNA-binding (53). Interestingly, a significant decrease of transcriptional activation relative to background level was seen in the presence of expressed E47. This could signify a dominant negative effect on protein function with an unknown molecular basis, and may potentially explain why this variant causes a different ocular phenotype compared to the investigated patient-derived variants.

Heterodimerization stimulates proteasome-dependent degradation

Co-expression of ATOH7 protein variants and E47 showed a significant reduction in protein amounts, which was abolished by the proteasome inhibitor MG-132 (Fig. 3). Interestingly, patient variant proteins, and to a lesser extent the previously characterized loss-of-function variant p.(Asn46His) and the synthetic variant p.(Ala59Gly), displayed an accelerated proteasome-dependent turnover in the presence of E47 (Fig. 4), suggesting an additional mechanism by which ATOH7 variants may show reduced function *in vivo*.

Proteasome-mediated degradation of ubiquitinated bHLH factors has been observed in previous studies (55). Dimerization of several human bHLH proteins, including E47, with the C. Elegans HLH-2 has been described as inducing dimerization-dependent proteasomal degradation (56). However, compromising protein dimerization by mutating important helix 1 residues abolished the dimerization-dependent degradation, in contrast to our findings. It is possible that although abolished dimerization leads to increased bHLH monomer stability, reduced but retained dimerization may lead to the opposite effect due to distorted dimer structure or simply to reduced binding of chromatin. The impact of bHLH dimerization on protein degradation may indeed depend on multiple factors. A published study reported greatly increased stability of bHLH DNA-binding inhibitor proteins (ID proteins) when forming heterodimers with E47 (57). The precise mechanisms of how this selective degradation occurs in the case of the described *ATOH7* patient SNVs are yet to be elucidated.

ATOH7 mutations as genetic basis for an ocular phenotype dominated by optic nerve hypoplasia

Given the significance of *ATOH7* as an early retinal transcription factor specifying RGC fate, it is feasible that non-functional *ATOH7* mutations lead to a severe reduction in differentiated RGCs and therefore affect optic nerve development. Furthermore, we consider the observed anomalies of the retinal vasculature, including tortuosity and incomplete peripheral vascularization, to be an indirect consequence of reduced RGC differentiation. This is supported by the observation that the majority of RGCs in the human retina are generated in gestational weeks 7-9 (58), which is followed by the development of the primary retinal vasculature at the RNFL/RGC interface at 14-15 weeks of gestation (28). This differentiates our findings from exudative vitreoretinopathies, where the primary cause for the vascular manifestations is incomplete angiogenesis due to impacted Wnt and Norrin signaling (59).

In this report we present various characteristics of the addressed *ATOH7* patient SNVs that culminate in a complete loss of function, thus supporting the hypothesis that p.(Ala59Thr) and p.(Ala59Val) are mutations likely causative of the described eye phenotype. This statement is based on several observations:

1) The rare compound heterozygous *ATOH7* mutations segregate with ONH in an autosomal recessive pattern, 2) both mutations affect the well-conserved 59th amino acid residue within the functionally important bHLH domain of *ATOH7*, 3) the mutations are predicted deleterious by three different algorithms, 4) the mutations show significantly increased proteasomal degradation and reduction in protein levels, 5) heterodimerization with E47 is reduced and consequently E-box DNA-binding of the heterodimer is reduced or abolished, 6) complete loss of transcriptional activation induced through the E-box containing promoter, comparable to the previously established loss-of-function mutation p.(Asn46His). A

proposed schematic model of the functional consequences induced by the p.(Ala59) mutations is presented in figure 8.

As the mutant ATOH7 proteins are likely able to form heterodimers but are functionally inactive, it is also possible that they act as dominant-negative proteins in analogy to the Id class of bHLH factors (60). The effects of the described *ATOH7* mutations could thus have a more global effect on the developing retina beyond what it is possible to address in the present study. Although this report characterizes several key mechanisms by which loss of transcriptional function may occur in the described patient variants, it would be desirable to perform functional characterization in an appropriate developmental environment as opposed to observations based on transgene expression in a cell line. An animal model or hiPSC-derived retinal organoid would provide the benefit of addressing transcriptome and DNA target alterations, as well as the morphology of RGCs.

Molecular basis of foveal hypoplasia

Foveal hypoplasia (FVH) is a reduction in or absence of the foveal pit and foveal avascular zone (61). FVH may be diagnosed and graded based on OCT findings (30). Grade one FVH is characterized by a shallow foveal pit and the presence of visible extrusion of the inner retinal layers. In grade two FVH, the foveal pit is completely absent. Grade three FVH is similar to grade two, but without visible outer segment lengthening, whilst in grade four FVH it is not possible to visibly differentiate the presumed fovea from the parafovea (30). OCT examination of the father revealed a shallow foveal pit and continuity in the outer nuclear layer and outer segment, consistent with grade one FVH. Signs of FVH were also found in the visually affected siblings suffering from ONH, where the index patient displayed findings consistent with grade one FVH and the sister showed a total absence of foveal pit consistent with grade two FVH.

Several conditions have been associated with FVH, including ocular albinism, aniridia, and achromatopsia (62). Foveal hypoplasia may also present as an isolated trait, commonly in association with nystagmus and low vision, although asymptomatic cases as well as cases with minor vision deficits have been reported (63–65). Autosomal dominant FVH (OMIM #136520) is caused by mutations in *PAX6* (40). Although autosomal dominant FVH may occur in isolation, it is commonly associated with nystagmus and present in patients with aniridia or albinism (66) and sporadically in patients with presenile cataracts (67). Autosomal recessive FVH (OMIM #609218) is caused by *SLC38A8* mutations (51). A common feature in these patients is optic nerve decussation defects and anterior segment dysgenesis in the absence of albinism (68).

In a study examining OCT changes in association with ONH, over 80 % of the investigated cases of ONH also presented findings consistent with FVH (69). It is therefore most likely that FVH and the vascular abnormalities observed in the affected siblings share a common developmental background with ONH in the affected siblings. Conversely, FVH in the absence of ONH in the father may be due to a simple heterozygous *ATOH7* mutation, however we consider this unlikely as the remaining three unaffected family members are carrying heterozygous *ATOH7* variants affecting the same amino acid residue and the unaffected brother is carrying the particular *ATOH7* variant. FVH in the father may therefore be a result of an unknown independent gene mutation.

NGS data analysis revealed *OPA3* as a possible candidate for FVH. *OPA3* encodes an outer mitochondrial membrane protein implicated in mitochondrial fission, apoptosis, and regulation of lipid metabolism, however the exact function remains to be fully elucidated (70–72). High expression of *OPA3* in the brain, retina, optic nerve, and lens has been observed throughout mouse embryogenesis (73). Mutations in *OPA3* have been previously linked to autosomal recessive 3-methylglutaconic aciduria with optic atrophy and extrapyramidal

symptoms, also known as Costeff syndrome (74), as well as autosomal dominant optic atrophy 3 with cataract (75).

The observed *OPA3* SNV is shared between the father and the two affected siblings, however it is also present in the older unaffected sister. Although segregation of the *OPA3* SNV with FVH is inconsistent in this family, it may be possible that *OPA3* mutations cause FVH with incomplete penetrance, analogous to the incomplete penetrance described in autosomal dominant optic atrophy (76). An alternative possibility is that FVH occurs as a result of combined *OPA3* p.(Gly15Arg) and *ATOH7* p.(Ala59Val) variants. This specific combination of variants is present exclusively in the family members presenting FVH and would explain the absence of the FVH phenotype in the other family members.

Summary

The presented cases are the first report of compound heterozygous *ATOH7* mutations associated with a phenotype predominated by optic nerve hypoplasia. Additional findings include foveal hypoplasia, as well as vascular abnormalities, which may be a consequence of ONH or pleiotropic observations. Analysis of this gene should be performed in patients with bilateral ONH, despite previous controversial reports.

Materials and Methods

Optical coherence tomography and fundus imaging

Macular and circumpapillary optical coherence tomography (OCT) was performed under non-mydriatic conditions using a single Heidelberg Spectralis® device (Heidelberg Engineering GmbH, Heidelberg Germany; software version 6.9a) by one of two authors (JVMH, CG-K), both of whom were experienced in acquiring and analyzing OCT data. The following macula scan parameters were employed: high resolution (HR) mode; 31 horizontally-aligned sections separated by 45 µm covering a retinal area of 30˚ horizontally x 25˚ vertically; 15 Automatic Real-Time Tracking (ART) scans averaged per section; centration on the fovea or presumed fovea. Circumpapillary scans were acquired with the following scan parameters: HR mode; 12˚ scan diameter; 100 ART scans averaged; centration on the visible center of the optic nerve head. It was necessary to amend the precise OCT acquisition settings used (with the goal of reducing the time necessary to acquire OCT data) when scanning the index patient and her affected sister, as their reduced visual function (potentially exacerbated by their young age) resulted in poor or unstable fixation. Despite this pragmatic approach, it was not possible to acquire all OCT scans in both affected patients: in the index patient, only a macula scan could be obtained, and then only in the left eye; in the affected sister, a macula scan was successfully performed in the right eye only, and circumpapillary scans in both eyes, however the scan from the left eye was of insufficient quality (77) and was excluded from further analysis.

All OCT scans were inspected by a single author (JVMH), and the software-generated definitions of the inner limiting membrane (ILM) and Bruch's membrane verified and (when necessary) corrected for all sections of the OCT scan. Following this verification, the 1, 3, 6 mm Early Treatment of Diabetic Retinopathy Study (ETDRS) grid was centered upon the fovea or presumed fovea, and a measure of total macular volume (TMV; in mm^3) obtained

from the proprietary software supplied by Heidelberg Engineering. For the circumpapillary scans, the software-generated definition of the retinal nerve fiber layer (RNFL) was also verified and, when necessary, corrected; global RNFL thickness (averaged from superior, inferior, temporal, and nasal quadrants) was obtained from the proprietary software. Macula scans were automatically segmented, with author JVMH verifying and, when necessary, correcting the software-generated definitions of RNFL, the ganglion cell layer (GCL), and the inner plexiform layer (IPL). The macular scan of the index patient was judged to be of insufficient quality to reliably distinguish the retinal layers and was thus not segmented. Due to the difficulty in accurately distinguishing the border of GCL and IPL, these layers were aggregated and subsequently treated as one layer, the ganglion cell-inner plexiform layer (GCIPL) (78). Following verification of these intra-retinal boundaries, the 1, 2.22, 3.45 mm ETDRS grid was centered upon the fovea or presumed fovea, and GCIPL volume was quantified as the sum of the volumes (in mm^3) of GCL and IPL as obtained from the software provided by Heidelberg Engineering. Structural measures of the retinal layers distal to IPL were neither verified nor analyzed for the purposes of this study.

Wide-angle fundus imaging was performed on the affected sister only with the Optomap® (Optos, Dunfermline, United Kingdom).

Magnetic resonance imaging

MRI was performed on a 3-Tesla MR scanner (GE Signa MR750) with an 8-channel head coil. The MRI protocol comprised thin-slice (2.5 mm) T2-weighted fat-saturated fast spin-echo images of the orbits in coronal orientation.

Whole exome sequencing

WES was performed with venous blood DNA. Libraries were prepared according to Nextera Rapid Capture Exome protocol (Illumina, San Diego, CA, USA) to generate 75 bp paired-end

reads. Sequence reads alignment, indexing of the reference genome, and variant calling were performed using a pipeline based on BWA at the BaseSpace Onsite (Illumina, San Diego, CA, USA). Annotation of the variants was performed using Alamut-batch (Interactive Biosoftware, Rouen, France), and variants were visualized on Alamut Viewer 2.3 (Interactive Biosoftware, Rouen, France) and Integrative Genomics Viewer 2.6 (79) (Broad Institute and the Regents of the University of California, CA, USA).

In order to identify the most likely disease-causing variants, a variant filtering pipeline was utilized according to our previous publication (80). Filtering of variants was performed primarily on a set of genes associated with ONH and/or FVH according to Suppl. Table 1, and was also extended to a gene panel for eye diseases (https://www.medmolgen.uzh.ch/de/services/Hauptgene.html, accessed 01.07.2019) when applicable. Owing to the rare occurrence of ONH and FVH in the population, only variants with frequency below 1 % were chosen on dbSNP minor allele frequency, 1 000 Genomes, Exome Sequencing Projects and Exome Aggregation Consortium.

Polymerase chain reaction and Sanger sequencing

Polymerase chain reaction (PCR) targeting *ATOH7* exon one was performed by 2-fragment PCR. Fragment one was amplified in 25 µl total volume using 1 X Amplitaq Gold™ 360 Master Mix (Applied Biosystems, Foster City, CA, USA), 1 X 360 GC Enhancer, 0.4 µM primers (ATOH7_Ex1_for4 and ATOH7_Ex1_rev2; Suppl. Table 2). Cycling conditions were as follows: 95 °C for 15 min; 35 cycles of [95 °C for 1 min, 60 °C for 1 min, 72 °C for 2 min]; 72 °C for 10 min. Fragment two was amplified in 25 µl total volume using 1.25 U HOT FIREPol® DNA Polymerase (Solis Biodyne, Tartu, Estonia), 1 X reaction buffer B1, 1.5mM MgCl2, 0.2 mM dNTPs and 0.3 µM primers (ATOH7_Ex1_for2 and ATOH7_Ex1_rev; Suppl. Table 2). Cycling conditions were as follows: 98 °C for 2 min; 20 cycles of [98 °C for 10 s, 72 °C for 2 min]; 72 °C for 10 min. PCR targeting *OPA3* exon one was performed in 50

µl total volume using 5 U Phusion® High-Fidelity DNA Polymerase (New England Biolabs; Ipswich, MA, USA), 1 X GC buffer, 1 X S-solution (Solis BioDyne, Tartu, Estonia), 0.2 mM dNTPs and 0.5 µM primers (OPA3_F and OPA3_R; Suppl. Table 2). Cycling conditions were as follows: 98 °C for 2 min; 20 cycles of [98 °C for 10 s, 72 °C for 2 min]; 72 °C for 10 min.

Sanger sequencing was performed by BigDye Terminator 3.1 (Applied Biosystems, Foster City, CA, USA) according to the manufacturer's instructions using 3130xl Genetic Analyzer (Applied Biosystems, Foster City, CA, USA).

Cloning of expression vectors

Full-length coding sequence of wildtype *ATOH7* (NM_145178.3) was amplified from gDNA of a control patient by PCR in 50 µl total volume with 3 U Pfu® Polymerase (Promega, Madison, WI, USA), 1 X Pfu buffer, 0.16 mM dNTPs and 0.2 µM primers (ATOH7_CACC_FWD and ATOH7_STOP_REV; Suppl. Table 2). Cycling conditions were as follows: 95 °C for 2 min; 35 cycles of [95 °C for 45 s, 58 °C for 30 s, 72 °C for 3.5 min]; 72 °C for 10 min. Human *TCF3-E47* cDNA (NM_001136139) was de novo synthesized (OriGene, Rockville, MD, USA; cat. RC227647). Expression constructs were created by subcloning into pcDNA™3.1/nV5-DEST mammalian expression vector (Invitrogen, Carlsbad, CA, USA) expressing either N-terminal V5 tag or C-terminal c-Myc tag.

ATOH7 variants were constructed by site directed mutagenesis of pcDNA3.1-ATOH7 construct. PCR reactions were performed by Phusion® High-Fidelity DNA Polymerase as described earlier using mutagenesis primers (Suppl. Table 3). PCR products were purified by NucleoSpin® Gel and PCR Clean-up (Macharey Nagel, Oensingen, Switzerland), digested by DPNI (New England Biolabs, Ipswich, MA, USA) for 2 h and transformed in TOP10 competent cells (Thermo Fisher Scientific, Waltham, MA, USA). *ATOH7* variants were verified by Sanger sequencing after which *ATOH7* CDS was re-cloned into pcDNA3.1 vector to avoid possible vector mutations introduced by PCR.

Cell culture

Human Embryonic Kidney 293T cells (HEK293T) were cultured at 36.5 °C and 5 % CO_2 in Dulbecco's Modified Eagle Medium (Gibco, Waltham, MA, USA; cat. 41966-029), supplemented with 10 % Fetal Calf Serum (Eurobio, Courtaboeuf, France) and 1 % penicillin/streptomycin (Corning, Corning, NY, USA). Cells were split at 80-90 % confluence. 24 h prior to transfection, cells were seeded at a density of $5x10^4$ cells/cm^2. Transfections were performed using branched Polyethylenimine (PEI; Mw ~25 000; Sigma-Aldrich, St. Louis, MO, USA) in ratio PEI:DNA 3:1 unless otherwise stated. Cells were harvested 24 h post-transfection.

Immunocytochemistry

HEK293T were cultured on Poly-L-Lysine pre-coated 22 x 22 mm coverslips inserted into six-well plates. Each well was co-transfected with 1.5 µg of pcDNA3.1-V5-ATOH7 and 1.5 µg of either empty vector or pcDNA3.1-*TCF3*-c-Myc. A series of three washes with PBS were performed between each step. Cells were fixated in 4 % paraformaldehyde (PFA) diluted in phosphate buffered saline (PBS) for 15 min, followed by permeabilization in 0.01 % Triton X-100 diluted in PBS for 20 min. Blocking was performed in 5 % bovine serum albumin (BSA) solved in PBS for 30 min. Primary antibody incubation was performed at room temperature for 1 h using rabbit anti-V5 ab (1:200; Suppl. Table 4) and mouse anti c-Myc ab (1:200; Suppl. Table 4) diluted in blocking solution. Secondary antibody incubation was performed at room temperature for 1 h using Alexa Fluor® 488 goat anti-rabbit ab (1:1000; Suppl. Table 4) and Alexa Fluor® 647 goat anti-mouse ab, (1:1000; Suppl. Table 4) diluted in blocking solution. Coverslips were mounted onto slides using Fluoromount-G® (Southern Biotech, Birmingham, AL, USA) containing 4′,6-diamidino-2-phenylindole (DAPI). Samples were imaged using a Leica SP8 confocal microscope (Leica Microsystems, Wetzlar, Germany) at 60 X magnification.

Western blot

HEK293T were cultured in six-well plates. Each well was co-transfected with 1.5 µg of pcDNA3.1-V5-ATOH7 and 1.5 µg of either pcDNA3.1 vector or pcDNA3.1-*TCF3*-c-Myc. Cells were washed twice with PBS, scraped down, and centrifuged at 1 000 G. Cell pellets were resuspended in lysis buffer consisting of 50 mM Tris-HLC (pH7.5), 150 mM NaCl 0.5 % sodium deoxycholate, 0.1 % sodium dodecyl sulphate; 1 % triton X-100, 1 tabl./50ml cOmplete™ protease inhibitor cocktail (Roche; Basel, Switzerland) and incubated for 30 min. Whole cell lysate was centrifuged at 14 000 G for 10 min and supernatant was collected. Total protein concentration was measured using Pierce™ BCA Protein Assay Kit (Thermo Scientific, Waltham, MA, USA) and adjusted to 1 500 µg/ml. Samples were denatured by boiling in loading buffer (250 mM Tris, pH 6.8, 10 % sodium dodecyl sulphate, 50 % glycerol, 5 % β-mercapthoethanol, 0.5 % bromophenol blue) at 99 °C for 5 min. SDS-PAGE was performed in 12.5 % acrylamide gels. Electrophoresis was performed in SDS run buffer (125 mM tris, 0.96M glycine, 17.3 mM sodium dodecyl sulphate) at 200 V for 40 min. Gels were blotted onto PVDF western blotting membranes (Roche, Basel, Switzerland) in semi-dry condition using blotting buffer (48 mM tris, 3.92 mM glycine, 1.30 mM sodium dodecyl sulfate, 20 % methanol) at 15 V for 40 min. Blots were blocked in tris-buffered saline containing 5 % milk (TBS-T) overnight at 4 °C. Immunoblotting was performed by incubation in TBS-T with mouse anti-V5 (1:5000; Suppl. Table 4) or mouse anti-c-Myc ab (1:400; Suppl. Table 4) for 1 h and subsequent incubation with sheep anti-mouse HRP-conjugated ab (1:2000, Suppl. Table 4) for 1 h. Reprobing was performed by two 10 min incubations in stripping buffer (0.20 M glycine, 3.47 mM SDS, 1 % ml Tween-20, pH2.2) followed by blocking and immunostaining using rabbit anti-β tubulin ab (1:1000; Suppl. Table 4) and donkey anti-rabbit conjugated ab (1:2000, Suppl. Table 4). Western lightning plus-ECL (PerkinElmer, Waltham, MA, USA) was applied for 1 min to the blots and imaging was performed in Chemidoc XRS+ (Bio-Rad Laboratories, Hercules, CA, USA).

Quantification was performed using Image Lab 5.0 software (Bio-Rad Laboratories, Hercules, CA, USA). Relative protein expression was quantified by normalizing to β-tubulin and expressed as fold change relative to wildtype ATOH7. Means were calculated from the results of three independent measurements (n=3) +/- SD.

Cycloheximide chase assay

Cells were treated with proteasome inhibitor MG-132 (Calbiochem, San Diego, CA, USA) 20 h post-transfection at a final concentration of 20 mM. Cells not treated with MG-132 were supplemented with equal volume DMSO (Sigma-Aldrich, St. Louis, MO, USA). Cycloheximide (CHX; Sigma-Aldrich, St. Louis, MO, USA), was added 24 h post transfection at a final concentration of 100 µg/ml. Cells were collected at 0, 1, 2 and 4 h after CHX addition and western blot was performed according to the above described protocol. Relative protein expression was quantified by normalizing to β-tubulin and expressed as fold change relative to ATOH7 at time point zero. Means were calculated from the results of three independent experiments (n=3) +/- SEM. Linear regression was fitted for the time course of each variant ($dF1,11$, $p<0.001$). Assessment of statistical differences was performed by multiple comparisons of the regression slopes using one-way ANOVA corrected for multiple comparisons using Tukey's test and 95 % confidence intervals.

Protein-protein interaction enzyme-linked immunosorbent assay

Each incubation was preceded by rinsing wells three times with a wash buffer consisting of PBS containing 0.1 % Tween-20. Nunc MaxiSorp™ flat-bottom 96-well plates (Invitrogen; Carlsbad, CA, USA) were coated overnight at 4 °C with 2.5 µg/ml mouse anti c-Myc monoclonal antibody 9E10 (Suppl. Table 4) diluted in coating buffer (50mM carbonate/bicarbonate, pH 9.6). On the following day, unspecific binding sites were blocked by 2 h incubation at 37 °C with PBS containing 3 % bovine serum albumin (BSA).

HEK293T were transfected with 20 µg of either pcDNA-V5-ATOH7, pcDNA3.1-ATOH7-c-Myc or pcDNA3.1-*TCF3*-c-Myc construct. Samples were lysed in IP lysis buffer (25 mM Tris-HCl, pH 7.4, 150 mM NaCl, 1 % NP-40, 1 mM EDTA, 5 % glycerol, protease inhibitor cocktail) and centrifuged at 14 000 G for 10 min. Supernatant was collected and total protein concentration was normalized to 1 000 µg/ml using Pierce™ BCA Protein Assay Kit (Thermo Scientific, Waltham, MA, USA). Lysates containing c-Myc-tagged respectively V5-tagged recombinant protein were mixed 1:1 before incubation in prepared ELISA plates overnight at 4 °C. Primary antibody incubation was performed with rabbit anti-V5 polyclonal antibody (1:1000; Suppl. Table 4) diluted in wash buffer for 90 min at 37 °C. Secondary antibody incubation was performed with goat anti-rabbit HRP-conjugated antibody (1:1000; Suppl. Table 4) diluted in wash buffer for 1 h at 37 °C. Colorimetric detection was performed using 3,3′,5,5′-Tetramethylbenzidine (TMB; Sigma-Aldrich, St. Louis, MO, USA) and measured at 690 nm using ELx808™ Absorbance Microplate Reader (Bio-Tek, Bad Friedrichshall, Germany). Raw data consisted of kinetic velocity maxima calculated on 100 repeated absorbance scans interspaced by 5 s intervals of shaking. Each sample measurement was normalized to background measurements consisting of sample detection in plates without immobilized c-Myc-tagged dimerization protein. Results were presented as fold change relative to the no dimerization control consisting of V5-tagged wildtype ATOH7 and no immobilized c-Myc-tagged dimerization partner. Means were calculated from the results of three independent experiments, each with three technical replicate measurements (n=3) +/- SD.

DNA-protein interaction enzyme-linked immunosorbent assay

The following procedure is based on the protocol for protein-protein interaction ELISA. Coating with capture antibodies was substituted by 10 µg/ml streptavidin diluted in coating buffer. Biotinylated E-box DNA consisting of seven tandem E-box binding sites (CAGGTG)

and scrambled (scr) E-box dimers were prepared by incubating 0.5 µM of sense and 5-biotinylated antisense ssODNs (Suppl. Table 5) in STE buffer (100 mM NaCl; 10 mM Tris-Cl, pH 8.0; 1 mM EDTA) for 5 min at 95 °C and cooling at room temperature for 30 min. Wells were incubated with either E-box dimer or scr dimer solution for 1 h at 37 °C. Blocking and lysate preparation was performed as above. Samples were incubated by mixing lysate from ATOH7 expressing cells with either lysate from negative controls or lysate from E47 expressing cells. ssDNA from salmon testes (1:50; Sigma-Aldrich, St. Louis, MO, USA) was added to samples to reduced unspecific protein-DNA-binding. Primary antibody incubation consisting of mouse anti-V5 monoclonal antibody (Suppl. Table 4) for 90 min in 37 °C. Secondary antibody incubation consisting of sheep anti-mouse HRP-conjugated antibody (Suppl. Table 4) for 1 h in 37 °C. Each sample measurement was normalized to background measurements consisting of sample detection in plates without immobilized E-box DNA. Results were presented as fold change relative to scr control consisting of V5-tagged wildtype ATOH7 measured in plates containing immobilized scr E-box. Means represent three independent experiments each with three technical replicate measurements (n=3) +/- SD.

Dual luciferase assay

HEK293T were co-transfected with 43.75 ng of firefly luciferase vector pGL4.23 (Promega, Madison, WI, USA) containing seven tandem E-box binding sites (CAGGTG) inserted in front of a minimal promoter, 43.75 ng of renilla luciferase control plasmid pGL4.75 (Promega, Madison, WI, USA), 87.50 ng of pcDNA3.1-V5-ATOH7 construct, and 0.22 ng of either pcDNA3.1 vector or pcDNA3.1-*TCF3*-c-Myc in ratio PEI:DNA 4.5:1. Transcriptional activation was determined using Dual-Glo® Luciferase Assay System (Promega, Madison, WI, USA) according to manufacturer's manual. Measurements were performed in Luminoskan Ascent (Thermo Labsystems, Helsinki, Finland). Individual firefly luminescence measurements were divided by corresponding renilla luminescence measurements. Results

were presented as fold change relative to background control consisting of transfections of p.GL4.23/4.75 and empty pcDNA3.1 vector or pcDNA3.1-*TCF3*-c-Myc. Means represent three independent experiments each with four biological replicate measurements (n=12) +/- SD.

Statistical analysis

Calculations and figures were made in GraphPad PRISM v6.07 (GraphPad Software Inc., San Diego, CA, USA). Unless stated elsewhere, testing of significance was performed by two-way ANOVA comparing simple effects within columns, corrected for multiple comparisons using Šidák correction, and 95 % confidence intervals.

Acknowledgements

We would like to thank Peter Breitschmid and Anouk Scherrer at the Department of Ophthalmology, University Hospital of Zurich, for fundus photography of the patients. We thank Jordi Maggi at the Institute of Medical Molecular Genetics, University of Zurich, for technical support. We are grateful to the patients and their family for their voluntary participation. We acknowledge the Center for Microscopy and Image Analysis at the University of Zurich for their assistance and usage of equipment.

This work was supported by the University of Zurich. JVMH is supported by the Albert Bruppacher Stiftung und the OPOS Stiftung.

Conflict of Interest Statement

None declared.

References

1. Patel, L., McNally, R. J. Q., Harrison, E., Lloyd, I. C. and Clayton, P. E. (2006) Geographical Distribution of Optic Nerve Hypoplasia and Septo-optic Dysplasia in Northwest England. *J. Pediatr.*, **148**, 85–88.
2. Teär Fahnehjelm, K., Dahl, S., Martin, L. and Ek, U. (2014) Optic nerve hypoplasia in children and adolescents; prevalence, ocular characteristics and behavioural problems. *Acta Ophthalmol.*, **92**, 563–570.
3. Mohney, B. G., Young, R. C. and Diehl, N. (2013) Incidence and Associated Endocrine and Neurologic Abnormalities of Optic Nerve Hypoplasia. *JAMA Ophthalmol.*, **131**, 898.
4. Brodsky, M. C. (1994) Congenital optic disk anomalies. *Surv. Ophthalmol.*, **39**, 89–112.
5. Siatkowski, R. M., Sanchez, J. C., Andrade, R. and Alvarez, A. (1997) The clinical, neuroradiographic, and endocrinologic profile of patients with bilateral optic nerve hypoplasia. *Ophthalmology*, **104**, 493–496.
6. Azuma, N., Yamaguchi, Y., Handa, H., Tadokoro, K., Asaka, A., Kawase, E. and Yamada, M. (2003) Mutations of the PAX6 Gene Detected in Patients with a Variety of Optic-Nerve Malformations. *Am. J. Hum. Genet.*, **72**, 1565–1570.
7. Garcia-Filion, P., Epport, K., Nelson, M., Azen, C., Geffner, M. E., Fink, C. and Borchert, M. (2008) Neuroradiographic, Endocrinologic, and Ophthalmic Correlates of Adverse Developmental Outcomes in Children With Optic Nerve Hypoplasia: A Prospective Study. *Pediatrics*, **121**, e653–e659.
8. Kelberman, D. (2006) Mutations within Sox2/SOX2 are associated with abnormalities in the hypothalamo-pituitary-gonadal axis in mice and humans. *J. Clin. Invest.*, **116**, 2442–2455.
9. Chen, C. A., Yin, J., Lewis, R. A. and Schaaf, C. P. (2017) Genetic causes of optic nerve hypoplasia. *J. Med. Genet.*, **54**, 441–449.
10. Dattani, M. T., Martinez-Barbera, J.-P., Thomas, P. Q., Brickman, J. M., Gupta, R., Mårtensson, I.-L., Toresson, H., Fox, M., Wales, J. K. H., Hindmarsh, P. C., et al. (1998) Mutations in the homeobox gene HESX1/Hesx1 associated with septo-optic dysplasia in human and mouse. *Nat. Genet.*, **19**, 125–133.
11. McNay, D. E. G., Turton, J. P., Kelberman, D., Woods, K. S., Brauner, R., Papadimitriou, A., Keller, E., Keller, A., Haufs, N., Krude, H., et al. (2007) HESX1 Mutations Are an Uncommon Cause of Septooptic Dysplasia and Hypopituitarism. *J. Clin. Endocrinol. Metab.*, **92**, 691–697.
12. Tajima, T., Hattorri, T., Nakajima, T., Okuhara, K., Sato, K., Abe, S., Nakae, J. and Fujieda, K. (2003) Sporadic Heterozygous Frameshift Mutation of HESX1 Causing Pituitary and Optic Nerve Hypoplasia and Combined Pituitary Hormone Deficiency in a Japanese Patient. *J. Clin. Endocrinol. Metab.*, **88**, 45–50.
13. Thomas, P. Q. (2001) Heterozygous HESX1 mutations associated with isolated congenital pituitary hypoplasia and septo-optic dysplasia. *Hum. Mol. Genet.*, **10**, 39–45.
14. Bosch, D. G. M., Boonstra, F. N., Gonzaga-Jauregui, C., Xu, M., de Ligt, J., Jhangiani, S., Wiszniewski, W., Muzny, D. M., Yntema, H. G., Pfundt, R., et al. (2014) NR2F1 Mutations Cause Optic Atrophy with Intellectual Disability. *Am. J. Hum. Genet.*, **94**, 303–309.
15. Schilter, K., Schneider, A., Bardakjian, T., Soucy, J.-F., Tyler, R., Reis, L. and Semina, E.

(2011) OTX2 microphthalmia syndrome: four novel mutations and delineation of a phenotype. *Clin. Genet.*, **79**, 158–168.
16. Ragge, N. K., Brown, A. G., Poloschek, C. M., Lorenz, B., Henderson, R. A., Clarke, M. P., Russell-Eggitt, I., Fielder, A., Gerrelli, D., Martinez-Barbera, J. P., et al. (2005) Heterozygous Mutations of OTX2 Cause Severe Ocular Malformations. *Am. J. Hum. Genet.*, **76**, 1008–1022.
17. Slavotinek, A. M., Chao, R., Vacik, T., Yahyavi, M., Abouzeid, H., Bardakjian, T., Schneider, A., Shaw, G., Sherr, E. H., Lemke, G., et al. (2012) VAX1 mutation associated with microphthalmia, corpus callosum agenesis, and orofacial clefting: The first description of a VAX1 phenotype in humans. *Hum. Mutat.*, **33**, 364–368.
18. Brown, N. L., Kanekar, S., Vetter, M. L., Tucker, P. K., Gemza, D. L. and Glaser, T. (1998) Math5 encodes a murine basic helix-loop-helix transcription factor expressed during early stages of retinal neurogenesis. *Development*, **125**, 4821–4833.
19. Wang, S. W. (2001) Requirement for math5 in the development of retinal ganglion cells. *Genes Dev.*, **15**, 24–29.
20. Brown, N. L., Patel, S., Brzezinski, J. and Glaser, T. (2001) Math5 is required for retinal ganglion cell and optic nerve formation. *Development*, **128**, 2497–2508.
21. Reichman, S., Slembrouck, A., Gagliardi, G., Chaffiol, A., Terray, A., Nanteau, C., Potey, A., Belle, M., Rabesandratana, O., Duebel, J., et al. (2017) Generation of Storable Retinal Organoids and Retinal Pigmented Epithelium from Adherent Human iPS Cells in Xeno-Free and Feeder-Free Conditions. *Stem Cells*, **35**, 1176–1188.
22. Macgregor, S., Hewitt, A. W., Hysi, P. G., Ruddle, J. B., Medland, S. E., Henders, A. K., Gordon, S. D., Andrew, T., McEvoy, B., Sanfilippo, P. G., et al. (2010) Genome-wide association identifies ATOH7 as a major gene determining human optic disc size. *Hum. Mol. Genet.*, **19**, 2716–2724.
23. Ghiasvand, N. M., Rudolph, D. D., Mashayekhi, M., Brzezinski, J. A., Goldman, D. and Glaser, T. (2011) Deletion of a remote enhancer near ATOH7 disrupts retinal neurogenesis, causing NCRNA disease. *Nat. Neurosci.*, **14**, 578–586.
24. Keser, V., Khan, A., Siddiqui, S., Lopez, I., Ren, H., Qamar, R., Nadaf, J., Majewski, J., Chen, R. and Koenekoop, R. K. (2017) The Genetic Causes of Nonsyndromic Congenital Retinal Detachment: A Genetic and Phenotypic Study of Pakistani Families. *Investig. Opthalmology Vis. Sci.*, **58**, 1028.
25. Prasov, L., Masud, T., Khaliq, S., Mehdi, S. Q., Abid, A., Oliver, E. R., Silva, E. D., Lewanda, A., Brodsky, M. C., Borchert, M., et al. (2012) ATOH7 mutations cause autosomal recessive persistent hyperplasia of the primary vitreous. *Hum. Mol. Genet.*, **21**, 3681–3694.
26. Khan, K., Logan, C. V., McKibbin, M., Sheridan, E., Elçioglu, N. H., Yenice, O., Parry, D. A., Fernandez-Fuentes, N., Abdelhamed, Z. I. A., Al-Maskari, A., et al. (2012) Next generation sequencing identifies mutations in Atonal homolog 7 (ATOH7) in families with global eye developmental defects. *Hum. Mol. Genet.*, **21**, 776–783.
27. Lim, S.-H., Germain, E. St., Tran-Viet, K.-N., Staffieri, S., Marino, M., Dollfus, P. H., Nading, E. B., Crowe, S., Gole, G., Perdomo-Trujillo, Y., et al. (2014) Sequencing Analysis of the ATOH7 Gene in Individuals with Optic Nerve Hypoplasia. *Ophthalmic Genet.*, **35**, 1–6.
28. Provis, J. M. (2001) Development of the primate retinal vasculature. *Prog. Retin. Eye Res.*, **20**, 799–821.
29. Henthorn, P., McCarrick-Walmsley, R. and Kadesch, T. (1990) Sequence of the cDNA encoding ITF-1, a positive-acting transcription factor. *Nucleic Acids Res.*, **18**, 677–677.

30. Thomas, M. G., Kumar, A., Mohammad, S., Proudlock, F. A., Engle, E. C., Andrews, C., Chan, W.-M., Thomas, S. and Gottlob, I. (2011) Structural Grading of Foveal Hypoplasia Using Spectral-Domain Optical Coherence Tomography. *Ophthalmology*, **118**, 1653–1660.
31. Fares-Taie, L., Gerber, S., Chassaing, N., Clayton-Smith, J., Hanein, S., Silva, E., Serey, M., Serre, V., Gérard, X., Baumann, C., et al. (2013) ALDH1A3 Mutations Cause Recessive Anophthalmia and Microphthalmia. *Am. J. Hum. Genet.*, **92**, 265–270.
32. Stevens, E., Carss, K. J., Cirak, S., Foley, A. R., Torelli, S., Willer, T., Tambunan, D. E., Yau, S., Brodd, L., Sewry, C. A., et al. (2013) Mutations in B3GALNT2 Cause Congenital Muscular Dystrophy and Hypoglycosylation of α-Dystroglycan. *Am. J. Hum. Genet.*, **92**, 354–365.
33. Armour, C. M. and Allanson, J. E. (2007) Further delineation of cardio-facio-cutaneous syndrome: clinical features of 38 individuals with proven mutations. *J. Med. Genet.*, **45**, 249–254.
34. Oatts, J. T., Duncan, J. L., Hoyt, C. S., Slavotinek, A. M. and Moore, A. T. (2017) Inner retinal dystrophy in a patient with biallelic sequence variants in BRAT1. *Ophthalmic Genet.*, **38**, 559–561.
35. Moog, U., Bierhals, T., Brand, K., Bautsch, J., Biskup, S., Brune, T., Denecke, J., de Die-Smulders, C. E., Evers, C., Hempel, M., et al. (2015) Phenotypic and molecular insights into CASK-related disorders in males. *Orphanet J. Rare Dis.*, **10**, 44.
36. Schuurs-Hoeijmakers, J. H. M., Geraghty, M. T., Kamsteeg, E.-J., Ben-Salem, S., de Bot, S. T., Nijhof, B., van de Vondervoort, I. I. G. M., van der Graaf, M., Nobau, A. C., Otte-Höller, I., et al. (2012) Mutations in DDHD2, Encoding an Intracellular Phospholipase A1, Cause a Recessive Form of Complex Hereditary Spastic Paraplegia. *Am. J. Hum. Genet.*, **91**, 1073–1081.
37. Willer, T., Lee, H., Lommel, M., Yoshida-Moriguchi, T., de Bernabe, D. B. V., Venzke, D., Cirak, S., Schachter, H., Vajsar, J., Voit, T., et al. (2012) ISPD loss-of-function mutations disrupt dystroglycan O-mannosylation and cause Walker-Warburg syndrome. *Nat. Genet.*, **44**, 575–580.
38. Zollino, M., Marangi, G., Ponzi, E., Orteschi, D., Ricciardi, S., Lattante, S., Murdolo, M., Battaglia, D., Contaldo, I., Mercuri, E., et al. (2015) Intragenic KANSL1 mutations and chromosome 17q21.31 deletions: broadening the clinical spectrum and genotype–phenotype correlations in a large cohort of patients. *J. Med. Genet.*, **52**, 804–814.
39. Raffa, L., Matton, M.-P., Michaud, J., Rossignol, E., Decarie, J.-C. and Ospina, L. H. (2017) Optic nerve hypoplasia in a patient with a de novo KIF1A heterozygous mutation. *Can. J. Ophthalmol.*, **52**, e169–e171.
40. Azuma, N., Nishina, S., Yanagisawa, H., Okuyama, T. and Yamada, M. (1996) PAX6 missense mutation in isolated foveal hypoplasia. *Nat. Genet.*, **13**, 141–142.
41. El Chehadeh, S., Kerstjens-Frederikse, W. S., Thevenon, J., Kuentz, P., Bruel, A.-L., Thauvin-Robinet, C., Bensignor, C., Dollfus, H., Laugel, V., Rivière, J.-B., et al. (2017) Dominant variants in the splicing factor PUF60 cause a recognizable syndrome with intellectual disability, heart defects and short stature. *Eur. J. Hum. Genet.*, **25**, 43–51.
42. Lamers, I. J. C., Reijnders, M. R. F., Venselaar, H., Kraus, A., Jansen, S., de Vries, B. B. A., Houge, G., Gradek, G. A., Seo, J., Choi, M., et al. (2017) Recurrent De Novo Mutations Disturbing the GTP/GDP Binding Pocket of RAB11B Cause Intellectual Disability and a Distinctive Brain Phenotype. *Am. J. Hum. Genet.*, **101**, 824–832.
43. Ullah, E., Wu, D., Madireddy, L., Lao, R., Ling-Fung Tang, P., Wan, E., Bardakjian, T., Kopinsky, S., Kwok, P.-Y., Schneider, A., et al. (2017) Two missense mutations in SALL4

in a patient with microphthalmia, coloboma, and optic nerve hypoplasia. *Ophthalmic Genet.*, **38**, 371–375.
44. Reyes-Capó, D. P., Chen, F., Wilson, B., Tarshish, B., Ventura, C. V., Read, S. P., Negron, C. I. and Berrocal, A. M. (2018) Aggressive Posterior Retinopathy of Prematurity and a TUBA1A Mutation inde Morsier Syndrome. *Ophthalmic Surgery, Lasers Imaging Retin.*, **49**, 629–632.
45. Abdollahi, M. R., Morrison, E., Sirey, T., Molnar, Z., Hayward, B. E., Carr, I. M., Springell, K., Woods, C. G., Ahmed, M., Hattingh, L., et al. (2009) Mutation of the Variant α-Tubulin TUBA8 Results in Polymicrogyria with Optic Nerve Hypoplasia. *Am. J. Hum. Genet.*, **85**, 737–744.
46. Ejaz, R., Lionel, A. C., Blaser, S., Walker, S., Scherer, S. W., Babul-Hirji, R., Marshall, C. R., Stavropoulos, D. J. and Chitayat, D. (2017) De novo pathogenic variant in TUBB2A presenting with arthrogryposis multiplex congenita, brain abnormalities, and severe developmental delay. *Am. J. Med. Genet. Part A*, **173**, 2725–2730.
47. Kohl, S., Zobor, D., Chiang, W., Weisschuh, N., Staller, J., Menendez, I. G., Chang, S., Beck, S. C., Garrido, M. G., Sothilingam, V., et al. (2015) Mutations in the unfolded protein response regulator ATF6 cause the cone dysfunction disorder achromatopsia. *Nat. Genet.*, **47**, 757–765.
48. Thiadens, A. A. H. J., Somervuo, V., van den Born, L. I., Roosing, S., van Schooneveld, M. J., Kuijpers, R. W. A. M., van Moll-Ramirez, N., Cremers, F. P. M., Hoyng, C. B. and Klaver, C. C. W. (2010) Progressive Loss of Cones in Achromatopsia: An Imaging Study Using Spectral-Domain Optical Coherence Tomography. *Investig. Opthalmology Vis. Sci.*, **51**, 5952.
49. Liu, J. Y., Ren, X., Yang, X., Guo, T., Yao, Q., Li, L., Dai, X., Zhang, M., Wang, L., Liu, M., et al. (2007) Identification of a novel GPR143 mutation in a large Chinese family with congenital nystagmus as the most prominent and consistent manifestation. *J. Hum. Genet.*, **52**, 565–570.
50. Murro, V., Mucciolo, D. P., Sodi, A., Passerini, I., Giorgio, D., Virgili, G. and Rizzo, S. (2019) Novel clinical findings in autosomal recessive NR2E3-related retinal dystrophy. *Graefe's Arch. Clin. Exp. Ophthalmol.*, **257**, 9–22.
51. Perez, Y., Gradstein, L., Flusser, H., Markus, B., Cohen, I., Langer, Y., Marcus, M., Lifshitz, T., Kadir, R. and Birk, O. S. (2014) Isolated foveal hypoplasia with secondary nystagmus and low vision is associated with a homozygous SLC38A8 mutation. *Eur. J. Hum. Genet.*, **22**, 703–706.
52. Dennis, D. J., Han, S. and Schuurmans, C. (2019) bHLH transcription factors in neural development, disease, and reprogramming. *Brain Res.*, **1705**, 48–65.
53. Longo, A., Guanga, G. P. and Rose, R. B. (2008) Crystal Structure of E47−NeuroD1/Beta2 bHLH Domain−DNA Complex: Heterodimer Selectivity and DNA Recognition. *Biochemistry*, **47**, 218–229.
54. Voronova, A. and Baltimore, D. (1990) Mutations that disrupt DNA binding and dimer formation in the E47 helix-loop-helix protein map to distinct domains. *Proc. Natl. Acad. Sci.*, **87**, 4722–4726.
55. Nie, L. (2003) Notch-induced E2A ubiquitination and degradation are controlled by MAP kinase activities. *EMBO J.*, **22**, 5780–5792.
56. Sallee, M. D. and Greenwald, I. (2015) Dimerization-driven degradation of C. elegans and human E proteins. *Genes Dev.*, **29**, 1356–1361.
57. Bounpheng, M. A., Dimas, J. J., Dodds, S. G. and Christy, B. A. (1999) Degradation of Id proteins by the ubiquitin-proteasome pathway. *FASEB J.*, **13**, 2257–2264.

58. Pacal, M. and Bremner, R. (2014) Induction of the ganglion cell differentiation program in human retinal progenitors before cell cycle exit. *Dev. Dyn.*, **243**, 712–729.
59. Sızmaz, S., Yonekawa, Y. and Trese, M. T. (2015) Familial Exudative Vitreoretinopathy. *Türk Oftalmol. Derg.*, **45**, 164–168.
60. Benezra, R., Davis, R. L., Lockshon, D., Turner, D. L. and Weintraub, H. (1990) The protein Id: A negative regulator of helix-loop-helix DNA binding proteins. *Cell*, **61**, 49–59.
61. Duke- Elder, S. (1963) *System of Ophthalmology*. The C. V. Mosby Company, St. Louis, MO.
62. Kondo, H. (2018) Foveal hypoplasia and optical coherence tomographic imaging. *Taiwan J. Ophthalmol.*, **8**, 181.
63. Querques, G., Prascina, F., Iaculli, C. and Noci, N. D. (2009) Isolated foveal hypoplasia. *Int. Ophthalmol.*, **29**, 271–274.
64. Giocanti-Aurégan, A., Witmer, M. T., Radcliffe, N. M. and D'Amico, D. J. (2014) Isolated foveal hypoplasia without nystagmus. *Int. Ophthalmol.*, **34**, 877–880.
65. Kirchner, I. D., Waldman, C. W. and Sunness, J. S. (2019) A series of five patients with foveal hypoplasia demonstrating good visual acuity. *Retin. Cases Brief Rep.*, **13**, 376–380.
66. Curran, R. E. and Robb, R. M. (1976) Isolated Foveal Hypoplasia. *Arch. Ophthalmol.*, **94**, 48–50.
67. O'Donnell, F. E. (1982) Autosomal Dominant Foveal Hypoplasia and Presenile Cataracts. *Arch. Ophthalmol.*, **100**, 279.
68. Al-Araimi, M., Pal, B., Poulter, J. A., van Genderen, M. M., Carr, I., Cudrnak, T., Brown, L., Sheridan, E., Mohamed, M. D., Bradbury, J., et al. (2013) A new recessively inherited disorder composed of foveal hypoplasia, optic nerve decussation defects and anterior segment dysgenesis maps to chromosome 16q23.3-24.1. *Mol. Vis.*, **19**, 2165–2172.
69. Pilat, A., Sibley, D., McLean, R. J., Proudlock, F. A. and Gottlob, I. (2015) High-Resolution Imaging of the Optic Nerve and Retina in Optic Nerve Hypoplasia. *Ophthalmology*, **122**, 1330–1339.
70. Huizing, M., Dorward, H., Ly, L., Klootwijk, E., Kleta, R., Skovby, F., Pei, W., Feldman, B., Gahl, W. A. and Anikster, Y. (2010) OPA3, mutated in 3-methylglutaconic aciduria type III, encodes two transcripts targeted primarily to mitochondria. *Mol. Genet. Metab.*, **100**, 149–154.
71. Ryu, S.-W., Jeong, H. J., Choi, M., Karbowski, M. and Choi, C. (2010) Optic atrophy 3 as a protein of the mitochondrial outer membrane induces mitochondrial fragmentation. *Cell. Mol. Life Sci.*, **67**, 2839–2850.
72. Wells, T., Davies, J. R., Guschina, I. A., Ball, D. J., Davies, J. S., Davies, V. J., Evans, B. A. J. and Votruba, M. (2012) Opa3, a novel regulator of mitochondrial function, controls thermogenesis and abdominal fat mass in a mouse model for Costeff syndrome. *Hum. Mol. Genet.*, **21**, 4836–4844.
73. Powell, K. A., Davies, J. R., Taylor, E., Wride, M. A. and Votruba, M. (2011) Mitochondrial Localization and Ocular Expression of Mutant Opa3 in a Mouse Model of 3-Methylglutaconicaciduria Type III. *Investig. Opthalmology Vis. Sci.*, **52**, 4369.
74. Anikster, Y., Kleta, R., Shaag, A., Gahl, W. A. and Elpeleg, O. (2001) Type III 3-Methylglutaconic Aciduria (Optic Atrophy Plus Syndrome, or Costeff Optic Atrophy Syndrome): Identification of the OPA3 Gene and Its Founder Mutation in Iraqi Jews. *Am. J. Hum. Genet.*, **69**, 1218–1224.

75. Reynier, P. (2004) OPA3 gene mutations responsible for autosomal dominant optic atrophy and cataract. *J. Med. Genet.*, **41**, e110–e110.
76. Lenaers, G., Hamel, C. P., Delettre, C., Amati-Bonneau, P., Procaccio, V., Bonneau, D., Reynier, P. and Milea, D. (2012) Dominant optic atrophy. *Orphanet J. Rare Dis.*, **7**, 46.
77. Tewarie, P., Balk, L., Costello, F., Green, A., Martin, R., Schippling, S. and Petzold, A. (2012) The OSCAR-IB Consensus Criteria for Retinal OCT Quality Assessment. *PLoS One*, **7**, e34823.
78. Cruz-Herranz, A., Balk, L. J., Oberwahrenbrock, T., Saidha, S., Martinez-Lapiscina, E. H., Lagreze, W. A., Schuman, J. S., Villoslada, P., Calabresi, P., Balcer, L., et al. (2016) The APOSTEL recommendations for reporting quantitative optical coherence tomography studies. *Neurology*, **86**, 2303–2309.
79. Robinson, J. T., Thorvaldsdóttir, H., Winckler, W., Guttman, M., Lander, E. S., Getz, G. and Mesirov, J. P. (2011) Integrative genomics viewer. *Nat. Biotechnol.*, **29**, 24–26.
80. Tiwari, A., Bahr, A., Bähr, L., Fleischhauer, J., Zinkernagel, M. S., Winkler, N., Barthelmes, D., Berger, L., Gerth-Kahlert, C., Neidhardt, J., et al. (2016) Next generation sequencing based identification of disease-associated mutations in Swiss patients with retinal dystrophies. *Sci. Rep.*, **6**, 28755.

Table 1 OCT measurements in family members. CRT: central macular thickness; GCIPL: ganglion cell and inner plexiform layer volume; LE: left eye; NA: not available; ONH: optic nerve head; RE: right eye; RNFL: retinal nerve fiber layer thickness; TMV: total macular volume (in mm^3). GCIPL volume is quantified in mm^3 over the 1, 2.22, 3.45 mm Early Treatment Diabetic Retinopathy Study (ETDRS) grid; TMV is quantified in mm^3 over the 1, 3, 6 mm ETDRS grid. RNFL is quantified as the average (global) thickness over 360˚ in µm. Gray shading: significantly reduced; black shading: thicker than normal. Foveal hypoplasia is graded according to the system proposed by Thomas et al. (30).

Patient	Age at examination (years)	Eye	TMV	CRT	GCIPL	RNFL	ONH diameter	Foveal hypoplasia
71877 (mother)	51	RE	8.64	243	0.79	87	1589 x 1883	NA
		LE	8.62	241	0.8	90	1505 x 1709	NA
71965 (father)	49	RE	9.32	300	0.85	104	1589 x 1754	1°
		LE	9.34	302	0.84	104	1635 x 1819	1°
72447 (sister)	18	RE	9.84	229	0.86	104	1570 x 1731	NA
		LE	9.68	230	0.87	105	1523 x 1674	NA
72484 (brother)	14	RE	9.32	232	0.83	123	1700 x 1623	NA
		LE	9.31	232	0.85	124	1613 x 1786	NA
72005 (index patient)	11	RE	NA	NA	NA	NA	NA (hypoplasia)	NA
		LE	7.53	284	NA	NA	NA (hypoplasia)	1°
71953 (affected sibling)	7	RE	7.28	278	0.33	28	NA (hypoplasia)	2°
		LE	NA	NA	NA	NA	NA (hypoplasia)	NA

Table 2 Described sequence variations and predicted impact on function. AA; amino acid; MAF: minor allele frequency (GnomAD); NFE: non-Finish European.

RefSeq	cDNA variation	AA variation	MAF (NFE)	SIFT	MutationTaster2	PolyPhen2
NM_145178.3(ATOH7)	c.175G>A	p.(Ala59Thr)	None	deleterious (score: 0.00)	disease-causing (p-value: 1)	probably-damaging (score: 1.00)
NM_145178.3(ATOH7)	c.176C>T	p.(Ala59Val)	$4x10^{-5}$	deleterious (score: 0.00)	disease-causing (p-value: 1)	probably-damaging (score: 1.00)
NM_001017989.2(OPA3)	c.43G>C	p.(Gly15Arg)	$1x10^{-5}$	deleterious (score: 0.01)	disease-causing (p-value: 1)	probably-damaging (score: 1.00)

Figure 1. A-B: Color fundus images showing a small and dysplastic optic disc and foveal hypoplasia associated with abnormal retinal vasculature in both eyes of index patient (A) and the affected sibling (B), together with pre-retinal gliotic tissue (B). Upper images are centered on the optic nerve; lower images are centered on the fovea; left images represent the right eye; right images represent the left eye. C-H: OCT images centered on the fovea show a shallow foveal pit and continuity in all retinal layers in the father (C) and the index patient (G), while the affected sister (H) shows absence of the foveal pit and continuity in all cell layers. The unaffected mother (D) and the older brother (E) and sister (F) show normal OCT findings. I-J: Coronal T2w fat-saturated images of patient showing severely hypoplastic optic nerves (arrows) with adjacent bright fluid signal within small optic nerve sheaths (I) and small optic nerves in the suprasellar cistern (arrows in J). The optic chiasm was not visualized. K-L: MRI findings in a healthy five-year-old boy (imaged following facial trauma) are presented for comparison, showing normal size of the optic nerves, optic nerve sheaths, and optic chiasm (arrows in K and L).

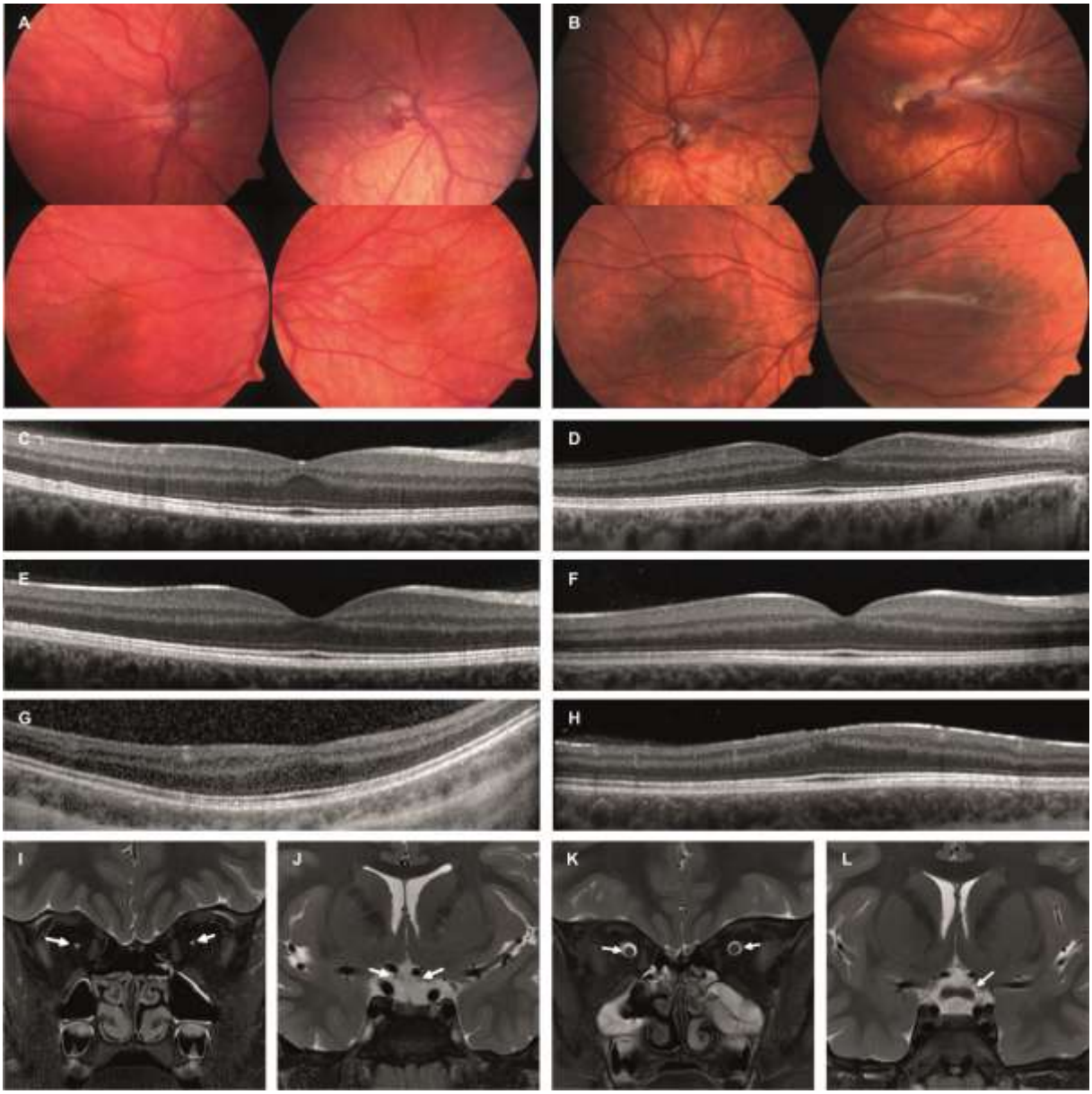

Figure 2. Compound heterozygous missense variants affecting the p.(Ala59) position of *ATOH7*. A: Pedigree of the family with two affected children showing segregation of compound heterozygous variants with ONH. B: Sanger DNA sequencing electropherograms depicting the compound heterozygous mutations in the two affected siblings. The DNA from the unaffected family members is heterozygous for one mutation (M1). C: Sequence alignment depicting the two biallelic *ATOH7* mutations in the index patient. Vertical bars represent sequencing depth (read coverage range shown in the image is 388-440 X). Each horizontal bar represents an aligned sequence; only mismatched nucleotides are shown in color. The BAM file format alignment is visualized by Integrative Genomics Viewer (IGV).

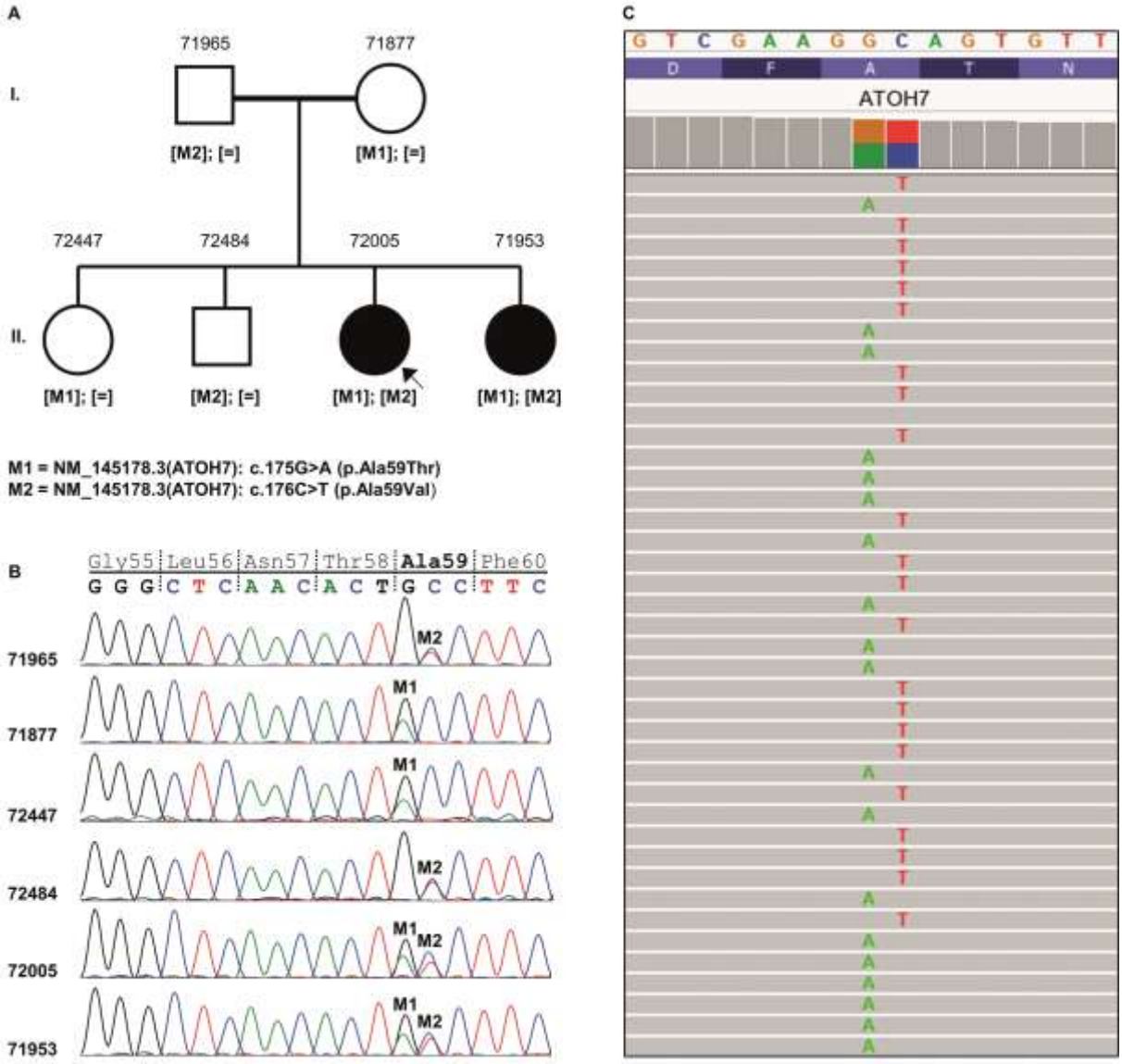

Figure 3. Semi-quantitative western blot of V5-tagged ATOH7 normalized to β-tubulin and presented as fold change relative ATOH7 WT. Patient variants display reduced protein amounts in the presence of the putative dimerization partner E47 due to proteasome-mediated degradation. Each bar represents mean ± SD of three separate experiments. A: Relative amount of V5-tagged ATOH7. B: Relative amount of V5-tagged ATOH7 in presence of co-expressed E47. C: Relative amount of V5-tagged ATOH7 in presence of proteasome inhibitor MG-132. D: Relative amount of V5-tagged ATOH7 in presence of co-expressed E47 and proteasome inhibitor MG-132. *, **, ***, **** represent p-values of < 0.05, $< 10^{-2}$, $< 10^{-3}$ and $< 10^{-4}$, respectively.

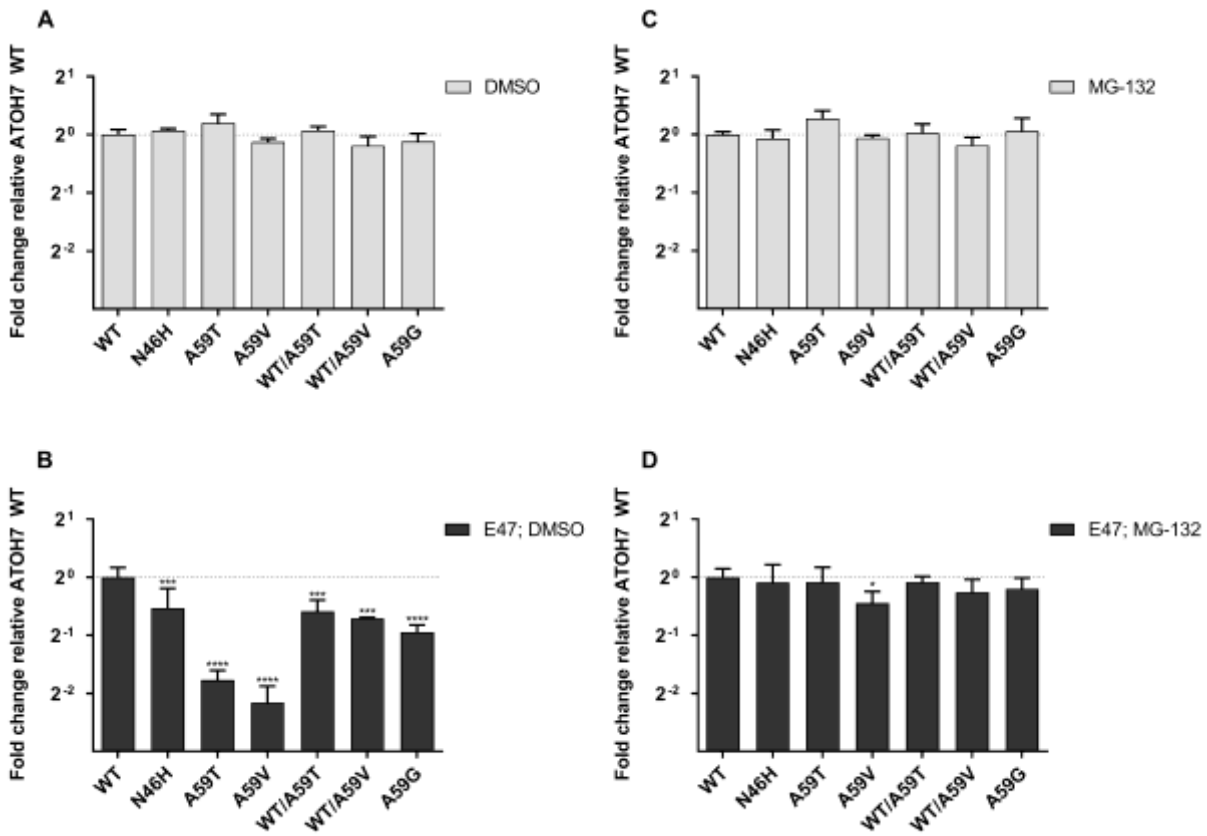

Figure 4. ATOH7 protein turnover quantified through semi-quantitative western blot of V5-tagged ATOH7 normalized to β-tubulin and presented as fold change relative to ATOH7 WT before CHX treatment (time point zero). Each point represents mean ± SEM of three separate experiments. Fitted lines represent linear regression of protein turnover, showing a negative relation between relative protein amount and time (dF1,11 and p<0.001 for all regressions). A: Turnover of ATOH7. B: Turnover of ATOH7 in the presence of co-expressed E47. C: Turnover of ATOH7 in the presence of proteasome inhibitor MG-132. D: Turnover of ATOH7 in the presence of co-expressed E47 and proteasome inhibitor MG-132. Statistical differences were tested by multiple comparisons of regression slopes. Star symbols (*) represent significance vs. ATOH7 WT and cross symbols (+) represent difference relative the previously published loss-of-function variant p.(Asn46His). *, **, ***, **** represent p-values of < 0.05, < 10^{-2}, < 10^{-3} and < 10^{-4}, respectively.

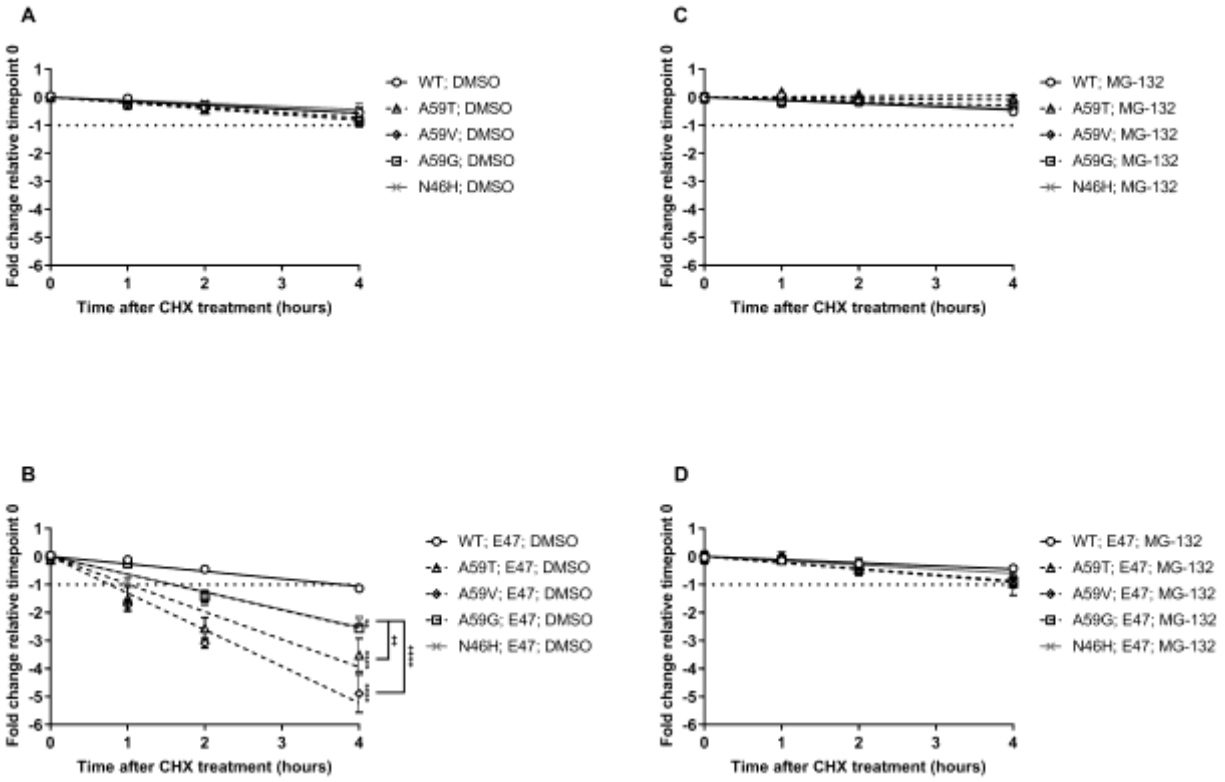

Figure 5. ATOH7 homo and heterodimerization quantified through protein-protein interaction ELISA. V5-tagged ATOH7 from cell lysate was bound by immobilized c-Myc-tagged dimerization partner. Results are normalized to background values (sample, no dimerization partner) and presented as fold change relative to untagged control (V5- tagged ATOH7 WT, untagged dimerization partner). Bars indicate mean of three independent experiments with three technical replicates ± SD. A: Dimerization with immobilized c-Myc-tagged ATOH7 WT. B: Dimerization with immobilized c-Myc-tagged ATOH7 variants. C: Dimerization with immobilized c-Myc-tagged E47. Asterisk symbols (*) represent significance vs. untagged control. *, **, ***, **** represent p-values of < 0.05, $< 10^{-2}$, $< 10^{-3}$ and $< 10^{-4}$, respectively.

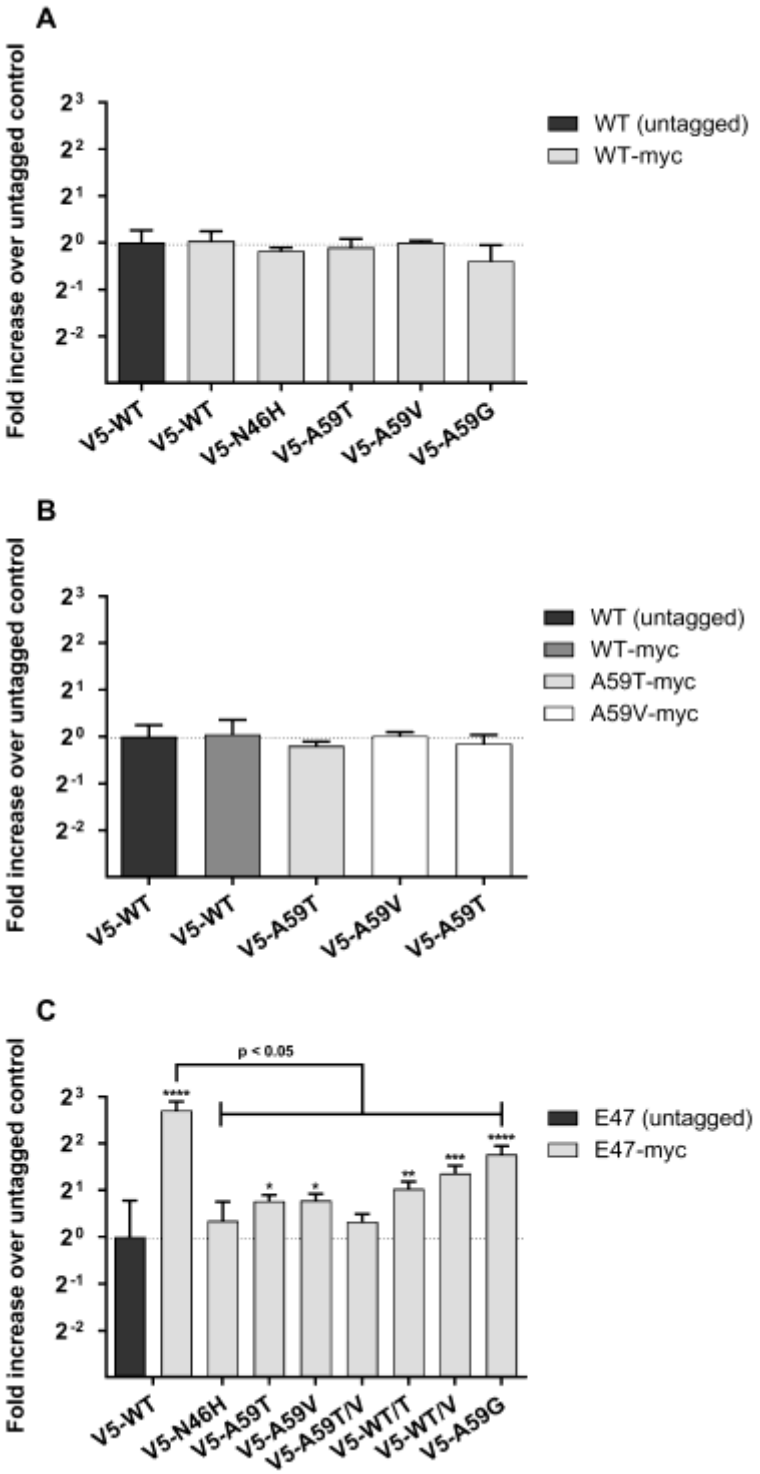

Figure 6. DNA-binding of ATOH7 quantified through DNA-protein interaction ELISA. V5-tagged ATOH7 from cell lysate was mixed with lysate containing c-Myc-tagged dimerization protein and bound by biotin-streptavidin immobilized E-box DNA. Results are normalized to background values (sample, no E-box DNA) and presented as fold change relative to scrambled control (ATOH7 WT, scrambled E-box). Each bar represents mean ± SD of three triplicates of three separate experiments. A: V5-ATOH7 DNA-binding in presence of c-Myc-tagged ATOH7. B: V5-ATOH7 DNA-binding in presence of c-Myc-tagged E47. Asterisk symbols (*) represent significance vs. scrambled control. *, **, ***, **** represent p-values of < 0.05, $< 10^{-2}$, $< 10^{-3}$ and $< 10^{-4}$, respectively. The pilcrow sign (¶) indicates significant reduction of variant p.(Asn46His) compared to all other ATOH7 variants ($p<0.0001$).

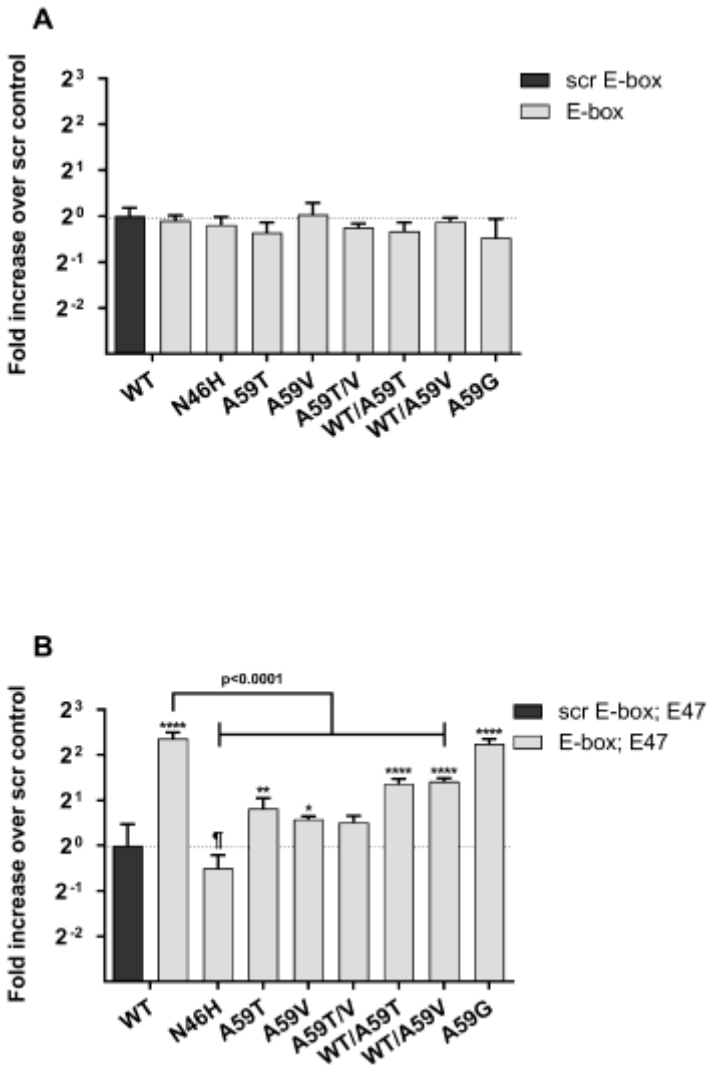

Figure 7. Transcriptional reporter gene activation by ATOH7 and its variants quantified through dual luciferase assay. HEK293T cells were transfected with plasmid firefly luciferase gene expressed under the control of an E-box containing minimal promoter, renilla luciferase under the control of a CMV-promoter, and pcDNA3.1 constructs containing *ATOH7* or *TCF3* under the control of a CMV-promoter. Firefly luminescence of each sample was normalized to renilla luciferase luminescence and is presented relative background control (no ATOH7 expression) in (A) and relative ATOH7 WT in (B). Bars indicate mean of three independent experiments with four biological replicates ± SD. Light grey bars represent luminescence in absence of E47; black bars represent luminescence in presence of E47. Asterisk symbols (*) represent significance vs. control without E47 expression; cross symbols (+) represent significance vs. control with E47 expression. *, **, ***, **** represent p-values of < 0.05, < 10^{-2}, < 10^{-3} and < 10^{-4}, respectively.

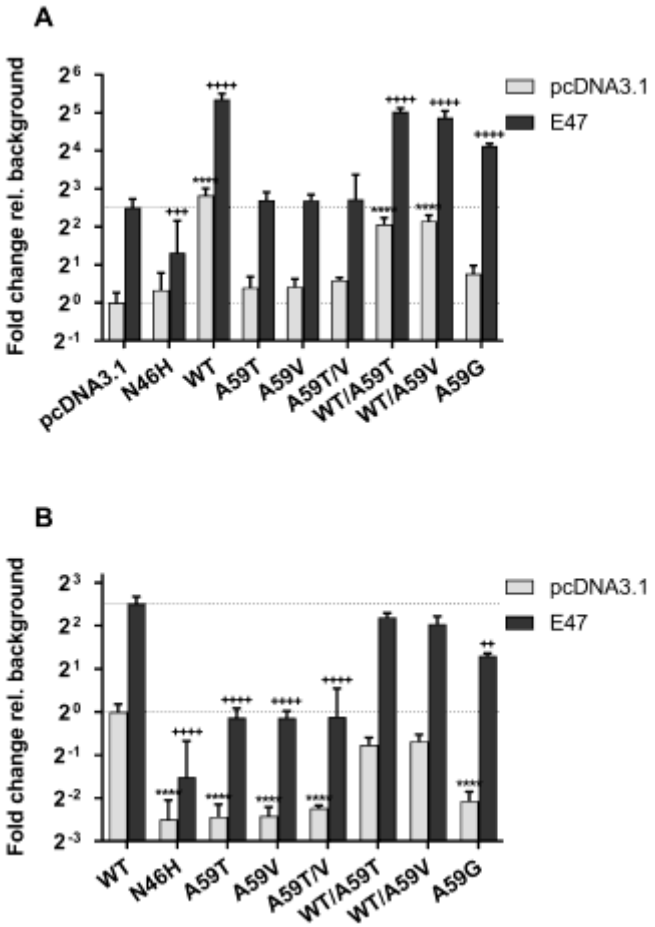

Figure 8. A schematic overview of proposed interactions in functional changes of the ATOH7 protein as a consequence of non-synonymous p.(Ala59) mutations. Plus (+) and minus (-) signs indicate up and down regulation, respectively; cross (X) indicates loss-of-function.

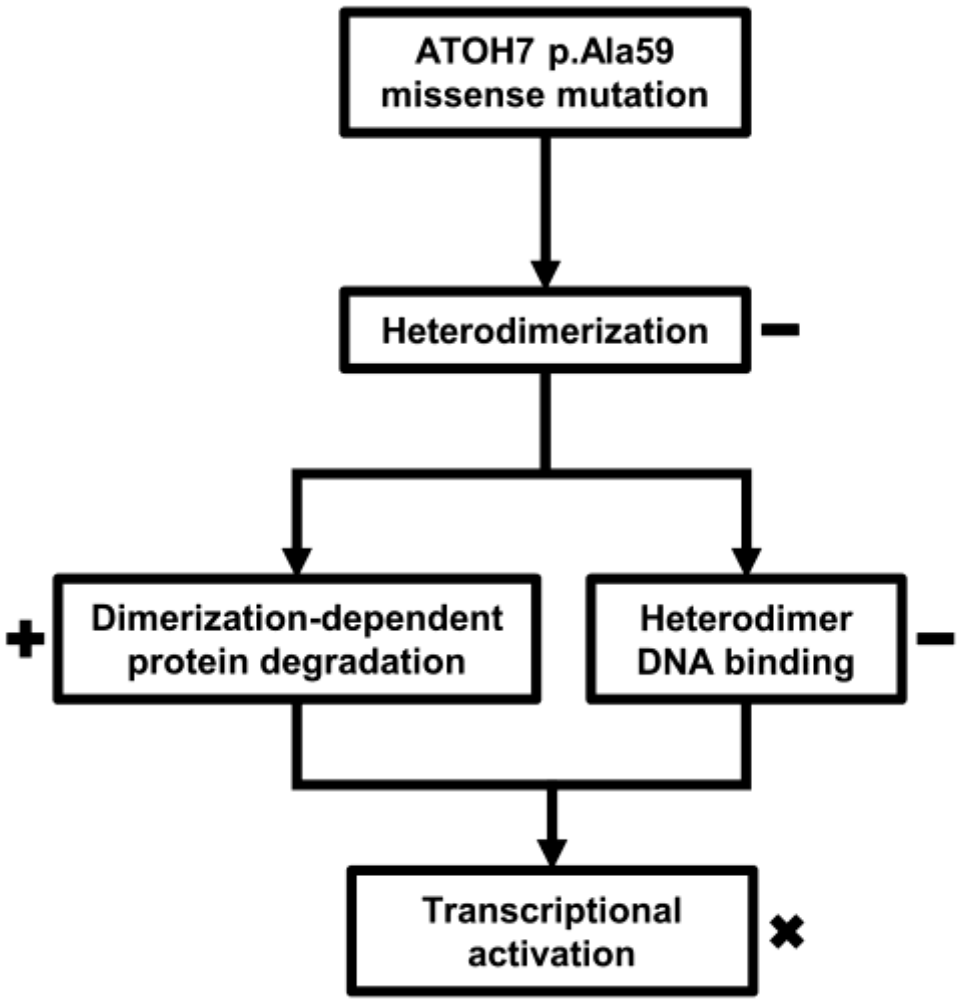

Abbreviations

Abbreviation	Meaning
ANOVA	analysis of variance
ATOH7*	atonal bHlH transcription factor 7
BBSOAS	Bosch-Boonstra-Schaaf Optic Atrophy Syndrome
BCA	bicinconinic acid assay
bHLH	basic helix-loop-helix
BWA	Burrows-Wheeler aligner
CHX	cycloheximide
DAPI	4′,6-diamidino-2-phenylindole
E47	transcription factor E2-alpha isoform E47
ELISA	enzyme-linked immunosorbent assay
EMSA	electrophoretic mobility shift assay
FVH	foveal hypoplasia
GCIPL	ganglion cell and inner plexiform layer
HEK293T	human embryonic kidney cell 293T
HESX1*	homeobox expressed in embryonic stem cells 1
HLH-2	helix-loop-helix 2
hiPSC	human induced pluripotent stem cell
Math5	mouse atonal homolog 5
MRI	magnetic resonance imaging
NCRNA	nonsyndromic congenital retinal nonattachment
NEUROD1	neuronal differentiation 1
NR2F1*	nuclear receptor subfamily 2 group F member 1
OCT	optical coherence tomography
OMIM	online mendelian inheritance in man
ONA	optic nerve aplasia
ONH	optic nerve hypoplasia
OTX2*	orthodenticle homeobox 2
OPA3*	optic atrophy 3
PAX6*	paired box 6
PBS	phosphate-buffered Saline
PCR	polymerase chain reaction
PEI	polyethylenimine
PFA	paraformaldehyde
PFV	persistent fetal vasculature
PHPV	persistent hyperplasia of the primary vitreous

POU4F2*	POU class 4 homeobox
RetNet	Retinal information network
RGC	retinal ganglion cell
RNFL	retinal nerve fiber layer
RPC	retinal progenitor cell
scr	scrambled
SLC38A8*	solute carrier family 38 member 8
SNP	single nucleotide polymorphism
SNV	single nucleotide variant
SOX2*	sex determining region Y box 2
ssODN	single-stranded oligodeoxynucleotide
TBS	tris-buffered saline
UTR	untranslated region
VAX1*	ventral anterior homeobox 1
WES	whole exome sequencing

* Refers to the gene when italicized, otherwise refers to the protein.